nature physics

Article

https://doi.org/10.1038/s41567-025-02917-6

Topological excitonic insulator with tunable momentum order

Received: 11 October 2024

Accepted: 11 April 2025

Published online: 11 July 2025

Check for updates

Md Shafayat Hossain[1,22,23] ✉, Zi-Jia Cheng[1,23], Yu-Xiao Jiang[1,23], Tyler A. Cochran[1,23], Song-Bo Zhang[2,3,23], Huangyu Wu[4,5,23], Xiaoxiong Liu[3,6,7,8,9], Xiquan Zheng[10], Guangming Cheng[11], Byunghoon Kim[1], Qi Zhang[1], Maksim Litskevich[1], Junyi Zhang[12], Jinjin Liu[4,5], Jia-Xin Yin[1], Xian P. Yang[1], Jonathan D. Denlinger[13], Massimo Tallarida[14], Ji Dai[14], Elio Vescovo[15], Anil Rajapitamahuni[15], Nan Yao[11], Anna Keselman[16,17], Yingying Peng[10], Yugui Yao[4,5,18], Zhiwei Wang[4,5,18] ✉, Luis Balicas[19,20], Titus Neupert[3] & M. Zahid Hasan[1,11,21] ✉

Correlated topological materials often maintain a delicate balance among physical symmetries. Many topological orders are symmetry protected, whereas most correlated phenomena arise from spontaneous symmetry breaking. Cases where symmetry breaking induces a non-trivial topological phase are rare. Here we demonstrate the presence of two such phases in $Ta_2Pd_3Te_5$, where Coulomb interactions form excitons that condense below 100 K, one with zero and the other with finite momentum. We observed a full spectral bulk gap, which stems from exciton condensation. This topological excitonic insulator state spontaneously breaks mirror symmetries but involves a weak structural coupling. Scanning tunnelling microscopy shows gapless boundary modes in the bulk insulating phase. Their magnetic field response, together with theoretical modelling, indicates a topological origin. These observations establish $Ta_2Pd_3Te_5$ as a topological excitonic insulator in a three-dimensional crystal. Thus, our results manifest a unique sequence of topological exciton condensations in a bulk crystal, offering exciting opportunities to study critical behaviour and excitations.

In the pursuit of new collective phases of matter that exhibit intriguing quantum properties, one long-standing goal has been the realization of the excitonic insulator. This excitonic phase of matter, initially proposed in theoretical studies dating back to 1964, is an exotic state where excitons spontaneously form and undergo Bose–Einstein condensation in thermodynamic equilibrium[1–4]. This elusive phenomenon has attracted substantial attention due to its predicted phenomenology, such as dissipationless energy transport akin to a superfluid[5], electronic ferroelectricity[6] and superradiant emission[7]. Formally, the excitonic insulator shares similarities with superconductors, as both involve many-body effects beyond non-interacting electron theory and the spontaneous emergence of a condensate of paired fermions. For an excitonic insulator, the condensate is formed by excitons, which are bound electron–hole pairs[8,9]. Although an excitonic insulator is primarily driven by electronic interactions, it is often accompanied by a pronounced structural phase transition[3,10], leaving many experimental signatures ambiguous. For example, among the three-dimensional (3D) materials considered as potential excitonic insulators[11–16], the most promising candidate so far, Ta_2NiSe_5, experiences such a prominent structural phase transition[10,17–19]. Consequently, whether Ta_2NiSe_5, indeed, hosts an excitonic insulator state remains a subject of debate[10]. Conversely, two-dimensional systems, such as bilayer heterostructures under high magnetic fields[20–25] and materials like WTe_2 (refs. 26,27), have shown indications of exciton condensation. Exciton condensation has

A full list of affiliations appears at the end of the paper. ✉e-mail: shossain@seas.ucla.edu; zhiweiwang@bit.edu.cn; mzhasan@princeton.edu

been observed for WTe_2 exclusively in the monolayer form[26,27], whereas 3D WTe_2 is a metal without an energy gap[28,29]. Here, we report the discovery of an excitonic insulator phase in a 3D material $Ta_2Pd_3Te_5$, where the excitonic insulator transition is accompanied by a relatively weak (but non-zero) structural coupling that does not obscure the excitonic insulator physics. Our data for this material indicate that excitons spontaneously form and condense, thus developing a bulk-gapped excitonic insulator state. Notably, our study unveils that this correlated insulating state has a topological character, rendering $Ta_2Pd_3Te_5$ as a topological excitonic insulator hitherto unknown in a 3D material.

In a topological excitonic insulator, the exciton condensate opens a topological gap in the single-particle band spectrum. Excitons form due to the attractive Coulomb interaction between electrons and holes near the charge-neutral point, leading to a pairing instability of the Fermi surfaces and, thus, the opening of an energy gap. This results in a thermodynamic phase transition, corresponding to the condensation of excitons, where the system transitions from a high-temperature (semi)metal to a fully gapped low-temperature insulator characterized by a topological mean-field band structure. Although it is not uncommon for electronic correlations to open a charge gap (for example, BCS superconductors or Mott insulators), it is very rare for that gap to be topologically non-trivial, as in a topological excitonic insulator. In topological exciton insulators, the correlated gap is accompanied by gapless topological boundary states. Although the topological excitonic insulator state has been theoretically suggested for Ta_2NiSe_5 (ref. 30), its presence remains inconclusive given that the experimental evidence for the excitonic insulator state in Ta_2NiSe_5 is itself still under debate. It is, therefore, desirable to find other materials that could host a topological excitonic insulator phase. In so doing, we demonstrate that $Ta_2Pd_3Te_5$ offers a unique competition between two symmetry-distinct topological excitonic insulator phases (with broken mirror symmetry and with or without broken translation symmetry). The accessibility of the resulting transition opens opportunities for studying critical behaviour and emergent excitations that link topology and symmetry breaking. Along these lines, our spectroscopic investigations reveal the tunable nature of the translation breaking under a magnetic field.

Our investigation began by characterizing the atomic structure of $Ta_2Pd_3Te_5$, which has an orthorhombic phase with the space group *Pnma* (No. 62) (Fig. 1a,b)[31,32]. The unit cell comprises two $Ta_2Pd_3Te_5$ monolayers that are stacked along the *a* axis through weak van der Waals interactions. Each monolayer encompasses a Ta–Pd mixed layer sandwiched between two Te layers. To confirm the pristine atomic structure of our $Ta_2Pd_3Te_5$ sample, we conducted detailed atomic imaging on the (010) and (001) surfaces using scanning transmission electron microscopy (STEM) (Extended Data Fig. 1). The results obtained confirm the expected lattice parameters of $Ta_2Pd_3Te_5$, with values of $a = 14.08$ Å, $b = 3.72$ Å and $c = 18.66$ Å, which are consistent with previous investigations[31,32]. Elemental mapping with an energy-dispersive X-ray detector (Extended Data Fig. 2) found unperturbed atomic layers, which verified the structural integrity and composition of $Ta_2Pd_3Te_5$. Furthermore, selected-area electron diffraction patterns acquired at temperatures of 290 K (top) and 90 K (bottom) (Extended Data Fig. 1) exhibited identical crystal symmetries and did not detect any structural phase transition in $Ta_2Pd_3Te_5$ within this temperature range. Refer to Extended Data Fig. 3 for the X-ray diffraction results elaborated on below. Atomically resolved scanning tunnelling microscopy (STM) topographic measurements revealed a freshly cleaved $Ta_2Pd_3Te_5$ (100) surface comprising quasi-one-dimensional atomic chains extending along the *b* axis (Fig. 1c), which corroborates the expected atomic structure. The lattice constants obtained from the STM topography are $b = 3.7$ Å and $c = 18.6$ Å. These values match our STEM results ($b = 3.72$ Å and $c = 18.66$ Å) and the crystallographic structure model ($b = 3.713$ Å and $c = 18.63$ Å). Furthermore, the angle between the *b* and *c* axes seems to be approximately 90°, which is consistent with the crystallographic structure for $Ta_2Pd_3Te_5$ and our STEM results.

Having identified a pristine surface, we conducted spectroscopic measurements. The spatially averaged differential conductance (dI/dV) spectra exhibited the temperature-dependent characteristics of gap formation (Fig. 1d). At higher temperatures ($T \gtrsim 100$ K), the system exhibited a gapless, semimetallic state, as evident from the nearly V-shaped dI/dV spectrum with a low but non-zero local density of states at the Fermi energy (E_F). However, an insulating gap (Extended Data Fig. 4) emerged at $T \lesssim 100$ K. The gap gradually increased in magnitude when the sample was cooled (Fig. 1e); see also Supplementary Notes 5 and 6. The development of this insulating energy gap could also be seen with angle-resolved photoemission spectroscopy (ARPES) by exploiting matrix-element selection effects and temperature control (Supplementary Notes 1–3 and Supplementary Figs. 1–3).

To understand the anomalous semimetal-to-insulator transition, we conducted polarization-dependent ARPES measurements. This technique leverages linearly polarized X-rays to provide a symmetry fingerprint of the electronic states[19,33]. Specifically, band hybridization between bands of distinct orbital characters is detectable through a change in the photoemission intensity for certain light polarizations. We oriented the sample such that the Γ_0–Z_0 path lies within the scattering plane, which ensured that photoelectrons emitted from the Γ point were free from any experimental asymmetry. We measured the energy–momentum cut along the Γ_0–Y_0 path with s and p polarizations at both 330 and 10 K. The results are summarized in Fig. 2. Here, s and p designate light with an electric field perpendicular or parallel to the plane of incidence, respectively.

At $T = 330$ K, the ARPES spectra measured with p polarization primarily show one parabolic conduction band (CB1) and an M-shaped hole-like valence band (VB1) (Fig. 2a). The bottom of CB1 was at the Γ point and slightly below the Fermi level, leading to the (semi)metallicity of the crystal. Conversely, only a hole-like valence band (VB2) appeared under the s-polarized probing light (Fig. 2c). Intriguingly, when the temperature dropped to 10 K, the top of the VB2 band descended by 60 meV, whereas changes to the VB1 band were negligible. Additionally, a faint but discernible spectrum of the VB1 band emerged in the s-polarized spectra. These results rule out a rigid band shift and indicate the presence of orbital hybridizations.

Note that under the experimental geometry, the M_y symmetry still holds for the photoemission process. Moreover, under the free-electron final-state approximation, we can conclude that only bands with odd (even) M_y parity have a finite spectral weight under s- (p)-polarized light, as the mirror parity of the initial-state wavefunction must be consistent with the parity of the electron dipole interaction to have non-zero transition probabilities. As depicted in Fig. 2e, CB1 and VB1 have positive M_y parities, whereas VB2 has a negative mirror parity in the normal phase. Note that the extracted M_y parities are consistent with the first-principles calculations (Fig. 2f). However, at $T = 10$ K, the appearance of VB1 in both s- and p-polarized spectra indicates a breaking of the M_y symmetry in the insulating phase. Moreover, the pronounced shift in VB2 and CB1, when contrasted with the stability of VB1, points to hybridization at lower temperatures between the two states, indicating a direct-coupling interaction, that is, coupling between two states at the same momentum ($\mathbf{Q} = 0$, where $\mathbf{Q}$ represents the wavevector of the ordering). This also supports the breaking of the mirror symmetry, given the different M_y parities of these states in the normal phase. Additionally, the first-principles calculations reveal that VB2 and CB1 exhibit different M_x parities, further indicating the breaking of the M_x symmetry at low temperatures; see 'Broken symmetries due to the excitonic insulator transition' in Methods for the symmetry analysis.

Although electron–lattice interactions will generically induce a structural phase transition when exciton condensation breaks the mirror symmetries, contrasting our polarization-dependent ARPES measurements with bulk scattering probes revealed that the driving mechanism was electronic instead of structural. In fact, our

https://doi.org/10.1038/s41567-025-02917-6

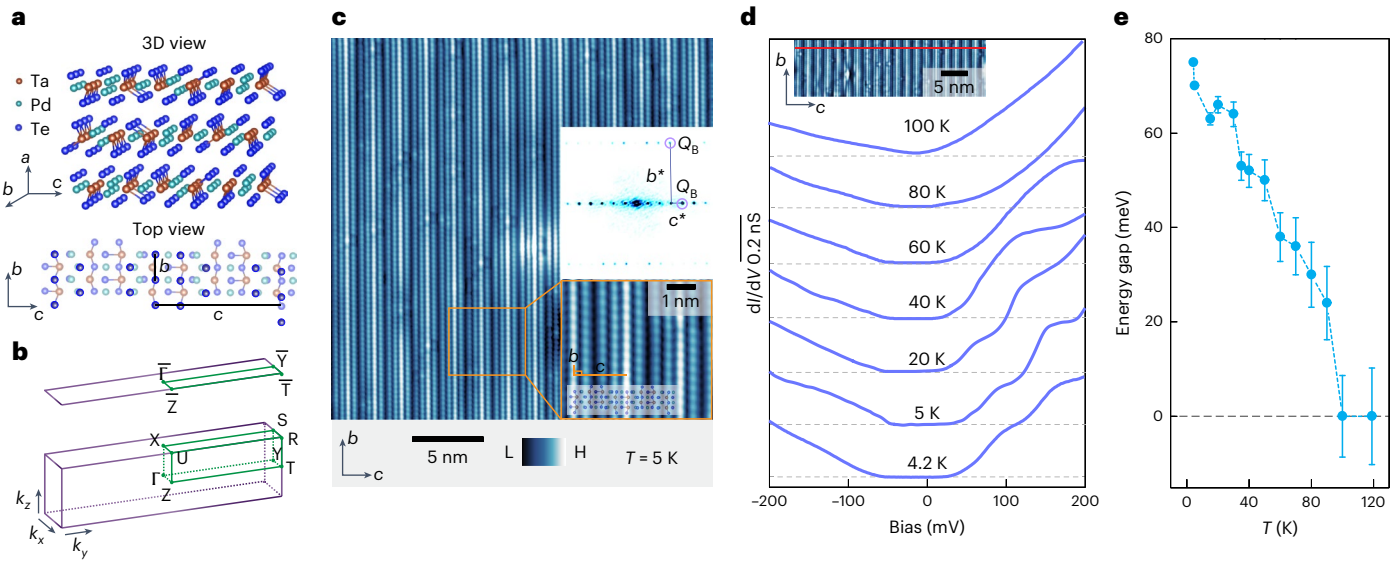

Fig. 1 | Real-space characterization of $Ta_2Pd_3Te_5$ showing the development of an insulating bulk gap around T = 100 K. a, Crystal structure (top) and top view of the (100) surface (bottom). The highlighted Te atoms are on the cleaved topmost plane of the (100) surface. The lattice constants b = 3.713 Å and c = 18.63 Å along the b–c plane are also indicated. **b**, Brillouin zone for $Ta_2Pd_3Te_5$ (bottom) and the surface Brillouin zone with surface normal perpendicular to the cleave plane (top). High-symmetry points and lines are marked in green. **c**, Atomically resolved STM topographic image of the (100) plane (tunnelling junction set-up: voltage bias between tip and sample V_{set} = 300 mV and tunnelling current I_{set} = 0.5 nA). Bottom inset, magnified view of the topographic image, showing lattice constants b = 3.7 Å and c = 18.6 Å and the approximately 90° angle between them, matching the crystallographic structure. The top view of the crystal structure (shown in **a**) is superimposed onto the image to indicate the atomic chains. Top inset, Fourier transform of the topographic image, indicating the Bragg peaks (Q_B) along the b and c axes. H and L in the colour bars denote high and low intensities, respectively. **d**, Spatially averaged energy-resolved tunnelling spectra obtained at various temperatures. The spectra were averaged over 20 curves along the red line marked in the topographic image (inset). Spectra for different temperatures are vertically offset for clarity. No gap was observed in the dI/dV spectrum at T = 100 K, whereas at T = 4.2 K, a sizeable insulating gap of approximately 75 meV emerged. **e**, Temperature dependence of the insulating gap. The gap was determined from the spectra in **d** as explained in 'Determining the energy gap from the tunnelling spectra' in Methods. The gap appeared around 100 K and increased with decreasing temperature. Vertical (error) bars indicate the thermal broadening energy for each data point.

structural measurements (electron and X-ray diffraction) show that any symmetry-breaking signatures occurring in conjunction with the gap formation were below our detection threshold (Extended Data Fig. 3, Supplementary Notes 8 and 9, and Supplementary Figs. 9 and 10). This is inconsistent with the possibility of symmetry breaking driven by the lattice. Furthermore, our specific heat measurements (Supplementary Note 10 and Supplementary Fig. 11) uncovered a weak anomaly near T = 100 K, which is difficult to reconcile with lattice-driven structural instabilities. Lattice-driven structural phase transitions usually lead to pronounced peaks, or lambda anomalies, in the specific heat due to the first-order nature of such transitions. Collectively, these measurements indicate that any changes in the lattice degrees of freedom were a secondary effect and that the mirror symmetry breaking detected by our ARPES measurements had an electronic origin. Therefore, the semimetal-to-insulator thermodynamic phase transition and the resultant mirror symmetry breaking stemmed from the formation of an exciton condensate. This condensate lowered the energy of the system by opening a gap, as seen in both the STM and ARPES measurements.

Our conclusion that there is an excitonic insulator state in $Ta_2Pd_3Te_5$ is based on detailed STM and ARPES measurements and is consistent with the findings of recent ARPES studies[34,35]. These observations in $Ta_2Pd_3Te_5$ contrast with the scenario for Ta_2NiSe_5, where a pronounced structural phase transition coincides with the exciton formation. This concurrence raises questions about the origin of the insulating gap in Ta_2NiSe_5: is it driven by electronic interactions or the lattice instability[10,17–19]? Recent studies indicate that the insulating gap in Ta_2NiSe_5, where a clear structural transition is detected, might primarily arise from structural instability instead of exciton condensation[10]. Conversely, possible structural changes in $Ta_2Pd_3Te_5$ due to exciton condensation were below our detection threshold, implying that the insulating gap in $Ta_2Pd_3Te_5$ primarily arises from electronic instability. Because the electronic and structural degrees of freedom were thermodynamically coupled, the breaking of electronic symmetry necessarily implies a structural anomaly (for example, a change in volume), although not necessarily a structural transition. The detection by ARPES of mirror symmetry breaking in $Ta_2Pd_3Te_5$ coupled with the absence of discernible structural changes in X-ray diffraction, electron diffraction and thermodynamic measurements indicate that the coupling between the electronic and structural order parameters is very weak in this material. A conclusive understanding of how the excitonic insulator transition impacts phonons in $Ta_2Pd_3Te_5$ will require detailed structural investigations.

Having unveiled the spontaneous condensation of excitons into a correlated insulating state, we investigated the topological properties of this correlated state. A hallmark of topology is the presence of gapless boundary states protected by time-reversal symmetry within the insulating bulk energy gap. To explore these boundary states, we conducted real-space investigations using STM, which allowed a direct, atomic-scale visualization with high spatial and energy resolution[36]. It has proven effective in identifying topological boundary states in various quantum materials[36–48]. Upon scanning a freshly cleaved $Ta_2Pd_3Te_5$ crystal, we observed a well-defined monolayer atomic step edge along the b axis, as identified by the topographic image and corresponding height profile in Fig. 3a. Notably, our spatially resolved spectroscopic imaging at T = 5 K revealed a pronounced edge state within the correlated insulating gap, as depicted by the differential conductance (dI/dV) maps at V = 0 and 30 mV in Fig. 3a (see Extended Data Fig. 5 for more results). To characterize the spatial profile of the edge state, we extracted a line profile from the dI/dV map, as illustrated in Fig. 3b. The line profile demonstrates an exponential decay of the edge state along the crystal side with a characteristic decay length of $r_0 \approx 1.6$ nm, indicating an exponential localization of the edge state.

https://doi.org/10.1038/s41567-025-02917-6

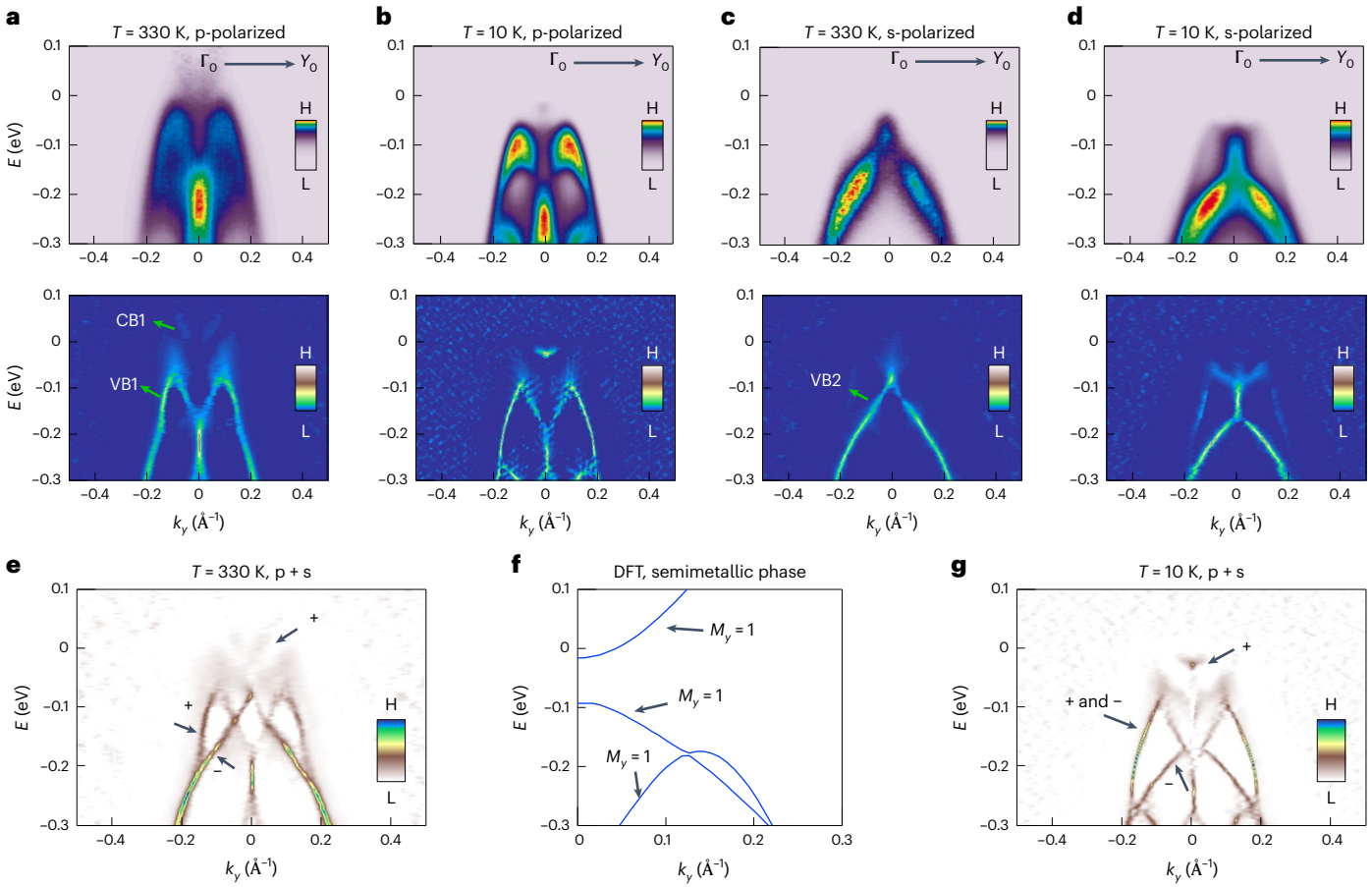

Fig. 2 | Signatures of interband hybridization and mirror symmetry breaking in the low-temperature electronic phase of $Ta_2Pd_3Te_5$. a–d, Experimental energy–momentum dispersions along the direction, captured using 54-eV photons with s and p polarizations at $T = 10$ or 330 K. Raw data are presented in the upper row, and the corresponding curvature plots are shown in the lower row. The conduction band (CB1) and two valence bands (VB1 and VB2) are highlighted by the green arrows. Data was acquired under the following conditions: $T = 330$ K (**a**) with p-polarized light; $T = 10$ K (**b**) with p-polarized light; $T = 330$ K with s-polarized light (**c**); and $T = 10$ K with s-polarized light (**d**). **e**, Full E versus k dispersion for the normal phase, obtained by combining s- and p-polarized data. **f**, Calculated band structure for monolayer $Ta_2Pd_3Te_5$ in its semimetallic phase. The calculated mirror-symmetry M_y parity (without considering spin–orbit coupling) for each band is also indicated, which matches the experimental results shown in **e**. **g**, Same as **e**, but for the low-temperature excitonic insulator phase. The eigenvalues for mirror symmetry M_y were extracted for each band based on their polarization dependencies and are summarized in **e** and **g**. Note that VB1 appears in both s- and p-polarization channels at low temperatures, indicating the breakdown of the M_y symmetry. Moreover, VB2 shifts substantially down to a deeper binding energy compared to VB1, ruling out the possibility of a rigid band shift and underscoring the presence of interaction-driven interband hybridization. Plus and minus signs indicate the mirror parities for each band. At the lowest temperatures, a distinct spectral feature emerges near the Γ_0 point in the ARPES curvature plot (**g**). This state has a positive M_y character and out-of-plane dispersion and follows the spectrum intensity distribution of CB1 at higher temperatures. (See the discussion in Supplementary Note 1.) H and L in the colour bars denote high and low intensities, respectively. DFT, density functional theory.

The edge state exhibited a steeper decay on the vacuum side. Furthermore, energy-resolved spectroscopic measurements conducted on the step edge (Fig. 3c) revealed a substantial dI/dV signal (orange curves) around the Fermi energy, whereas the dI/dV spectrum away from the step edge (violet curves) had an insulating gap. Note that the spectral dip of the Fermi energy of the edge state could possibly be attributed to Tomonaga–Luttinger liquid behaviour, a many-body ground state associated with one-dimensional bands, as reported for edge states in bismuthene[49] and Bi_4Br_4 (ref. 48), for instance.

Although edge modes have been observed in $Ta_2Pd_3Te_5$ (refs. 31,32), no clear evidence for their topological nature has been reported. To test the topological nature of the observed boundary state, we investigated its response to an external magnetic field. The magnetic field broke the time-reversal symmetry, which protected the gapless topological edge states. When a magnetic field perpendicular to the b–c plane was applied, we observed a substantial suppression of the dI/dV measured at the step edge. The field-dependent tunnelling spectra, shown for $B = 2$, 3 and 6 T in Fig. 3c, demonstrate the gradual formation of an insulating gap at the edge state. (The field-induced suppression of the edge state is also visualized in the dI/dV map under $B = 6$ T in Fig. 3d.) The emergence of this gap at the step edge bears resemblance to a Zeeman gap, which typically stems from the field-induced coupling of helical edge states in a time-reversal symmetric material[50–52]. Notably, a clear and reasonably linear increase of the energy gap in both the terrace (bulk) and the step edge was observed when we plotted the energy gap magnitude derived from the field-dependent tunnelling spectra as a function of the magnetic field (Fig. 3e), thus corroborating the anticipated behaviour of the Zeeman effect. By attributing the gap only to the Zeeman effect, we could estimate the Landé g-factors of the bulk and edge state, yielding values of 9 and 70, respectively. Note that these g-factor estimates also include the effect of orbital magnetization. Furthermore, because the bulk energy gap was due to interactions, its magnitude may have been affected by the magnetic field, leading to a nonlinear dependence of the gap on B that cannot be characterized by an effective g-factor alone. Overall, the observed edge state, initially gapless and located within the bulk insulating energy gap, underwent a transition to a gapped state when subjected to a time-reversal-symmetry-breaking perturbation, which provides

https://doi.org/10.1038/s41567-025-02917-6

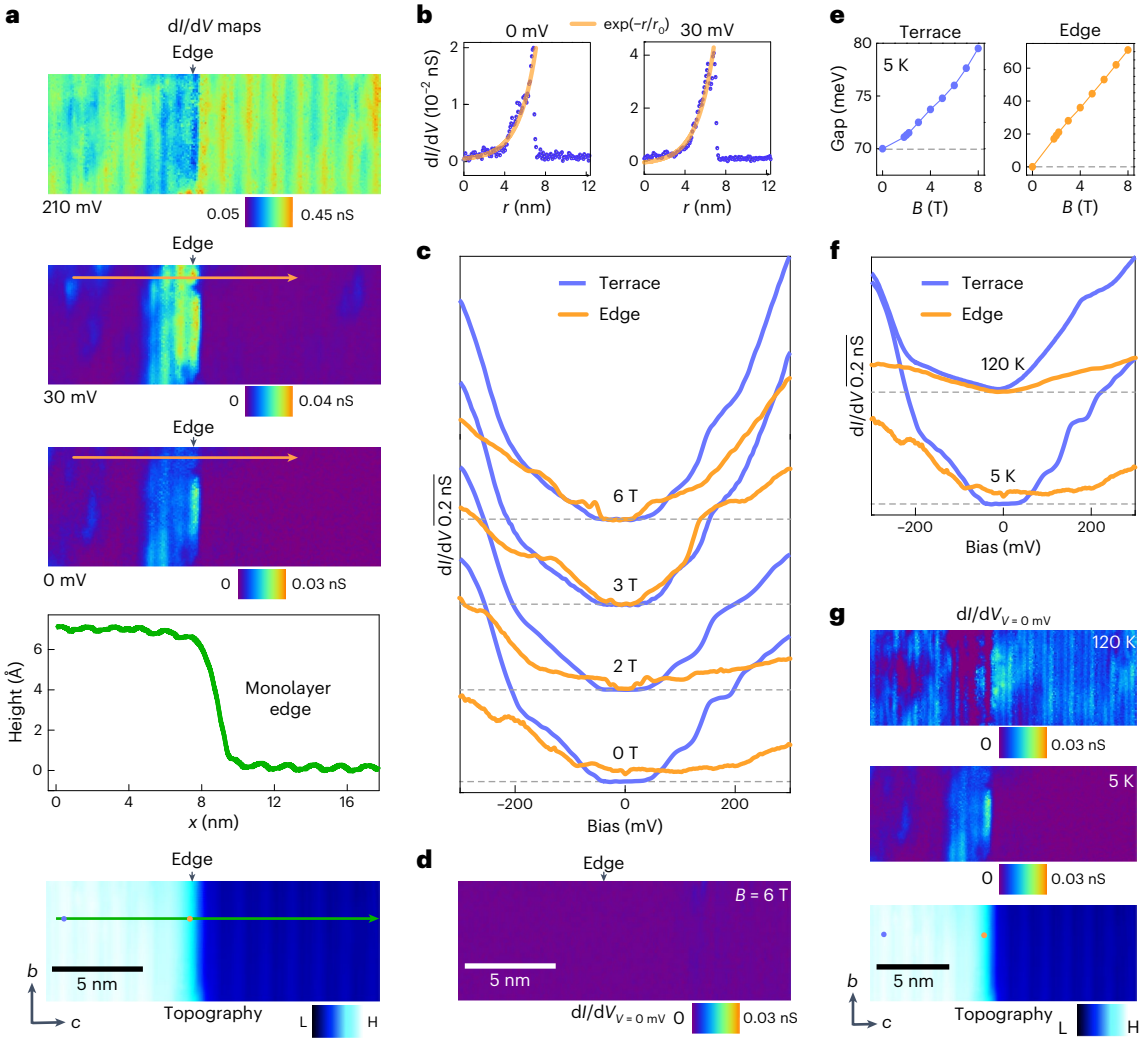

Fig. 3 | Topological nature of the insulating gap. a, d*I*/d*V* maps acquired at different bias voltages (the corresponding topography is shown at the bottom) around a monolayer step edge parallel to the *b* axis, measured at $T = 5$ K. The height profile taken perpendicularly to the *b* axis is also displayed. **b**, Intensity distribution of the differential conductance around the step edge captured at $V = 0$ and 30 mV. The corresponding location is marked by a green line on the topographic image in **a**, and the scan direction is indicated by the arrows. The orange curve is the exponential fit $\left(e^{-r/r_0}\right)$ of the decay of the state away from the step edge, with a fitted decay length (r_0) of 1.6 nm. **c**, Tunnelling spectra at locations away from the step edge and on the step edge measured under various magnetic fields. The orange and violet curves represent the differential spectra taken at the step edge and away from it, respectively. The corresponding spatial locations where the spectra are acquired are indicated by the colour-coded dots on the topographic image in **a** (bottom). Spectra at different magnetic fields were taken at the same locations and are vertically offset for clarity. Dashed horizontal lines mark zero d*I*/d*V* for different fields. **d**, d*I*/d*V* map at $B = 6$ T ($V = 0$ mV) taken in the same region as in **a**. **e**, Measured spectroscopic energy gaps at the terrace (left) and on the step edge (right) plotted as functions of the magnetic field. **f**, Tunnelling spectra at locations away from the step edge and on the step edge measured at temperatures $T = 120$ and 5 K. The spectra at the two temperatures were taken at the same locations and are vertically offset for clarity. Dashed horizontal lines mark zero d*I*/d*V* for the two temperatures. **g**, d*I*/d*V* maps at the Fermi energy ($V = 0$ mV) around a monolayer step edge parallel to the *b* axis measured at $T = 120$ and 5 K. The corresponding topography is shown at the bottom. The colour-coded dots overlaid on the topographic image correspond to the specific spatial locations where the d*I*/d*V* spectra in **f** were acquired. Tunnelling junction set-up: $V_{set} = 300$ mV, $I_{set} = 0.5$ nA and the modulation voltage used for the lock-in detection $V_{mod} = 2$ mV. H and L in the colour bars denote high and low intensities, respectively.

compelling evidence for its protection by the time-reversal symmetry, a characteristic hallmark of topological boundary states[53,54]; see Supplementary Notes 4 and 15–17 and Supplementary Fig. 17 for more results.

Additionally, we conducted temperature-dependent tunnelling measurements to examine the behaviour of the edge state as the bulk insulating gap closed above the excitonic insulator transition temperature. The results of these experiments, depicted in Fig. 3f, demonstrate that the insulating bulk gap and the prominent edge state observed at $T = 5$ K disappeared at $T = 120$ K. At $T = 120$ K, the bulk reverted to a gapless, semimetallic state, whereas the d*I*/d*V* magnitude of the edge state became suppressed with respect to the bulk. This temperature-dependent transition of the quantum state of the bulk and edge is also evident in the spatially resolved spectroscopic maps in Fig. 3g. At $T = 5$ K, the d*I*/d*V* maps taken at the Fermi energy display a pronounced state at the edge and no discernible state at the bulk, whereas at $T = 120$ K, the bulk states are more prominent with respect to the edge; see Extended Data Fig. 5 for more results.

The presence of a topological boundary mode within the correlated excitonic insulator energy gap indicates that the ground state of the material is a topological excitonic insulator. Next, we further cooled the sample to examine the excitonic state at lower temperatures. Figure 4a displays a large-area topographic image and corresponding d*I*/d*V* maps of the occupied side (−200 mV) and unoccupied side (100 mV) of the insulating gap at $T = 5$ K. As alluded to in

https://doi.org/10.1038/s41567-025-02917-6

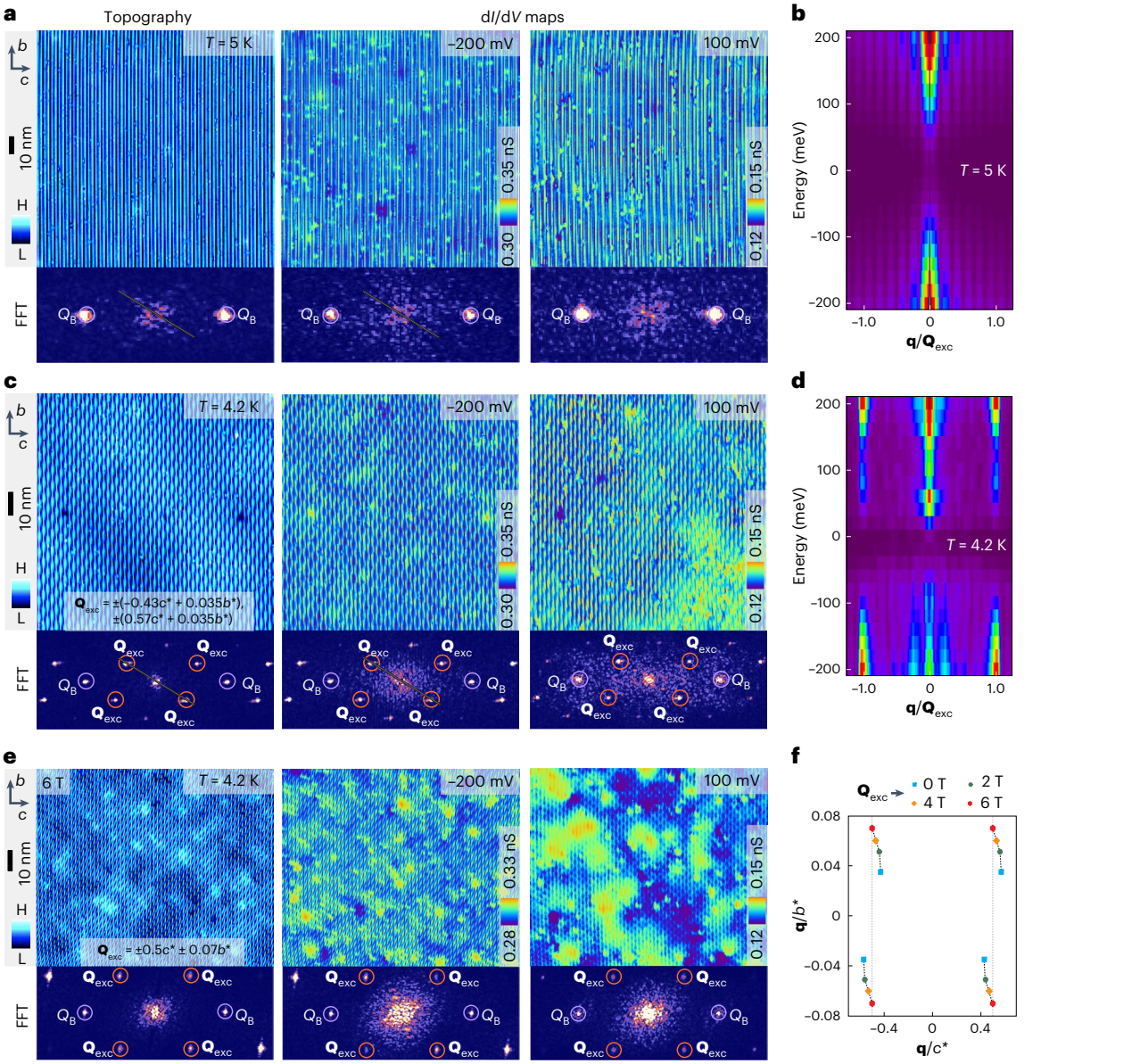

Fig. 4 | Secondary exciton instability with non-zero wavevector leading to translation symmetry breaking. a, Top, topography (left) and d*I*/d*V* maps acquired at the occupied ($V = -200$ mV) (middle) and unoccupied side ($V = 100$ mV) (right) of the insulating gap measured at $T = 5$ K. Bottom, corresponding Fourier transform images revealing well-developed Bragg peaks (purple circles). **b**, Energy dependence of the Fourier transform magnitude along the grey line in the Fourier transform images (the horizontal axis is normalized by $\mathbf{Q}_{exc}$, defined in **c**). **c**, Topography (left) and d*I*/d*V* maps acquired at $V = -200$ and 100 mV, measured at $T = 4.2$ K, showing a pronounced translation-symmetry-breaking order as revealed through the topographic and spectroscopic contrast. The Fourier transform images of the topography and the d*I*/d*V* maps shown on the bottom display well-defined wavevector peaks (orange circles) alongside the Bragg peaks (purple circles). The wavevector, $\mathbf{Q}_{exc} = \pm(-0.43c^* + 0.035b^*)$ and $\pm(0.57c^* + 0.035b^*)$. **d**, Energy-dependent Fourier transform magnitude along the line cut indicated with a grey line in the Fourier transform images showing the energy dependence of $\mathbf{Q}_{exc}$. The line cut position is the same as in **a**. Akin to the data in **b**, the horizontal axis here is also normalized by $\mathbf{Q}_{exc}$. In contrast to the **b** data, however, a non-dispersing, well-developed peak intensity is seen at $\mathbf{q} = \mathbf{Q}_{exc}$ and at both sides of the insulating energy gap. The plots in **b** and **d** were constructed using voltage bias intervals of 20 meV and 12.5 meV, respectively. As such, these plots lack sufficient energy resolution to accurately reflect gap sizes at the respective temperatures. **e**, Top, topography (left) and d*I*/d*V* maps acquired at the occupied side ($V = -200$ mV) (middle) and unoccupied side ($V = 100$ mV) (right) of the energy gap, measured at $T = 4.2$ K under 6 T field, revealing the topographic and spectroscopic contrast associated with the translation-symmetry-breaking order. Bottom, Fourier transform images of the topography and the d*I*/d*V* maps. Strikingly, here $\mathbf{Q}_{exc} = \pm(0.5c^* + 0.07b^*)$ is different from $\mathbf{Q}_{exc}$ under zero magnetic field. **f**, Scatter plot highlighting the magnetic field tunability of $\mathbf{Q}_{exc}$. Tunnelling junction set-up, $V_{set} = 300$ mV, $I_{set} = 0.5$ nA and $V_{mod} = 2$ mV. FFT, fast Fourier transform.

earlier discussions, in this zero-momentum exciton condensate, no superlattice modulations in the charge distribution were observed. Only the Bragg peaks are visible in the respective Fourier transform images (Fig. 4a,b). Strikingly, however, at an even lower temperature of $T = 4.2$ K, a secondary spontaneous electronic transition that does break translation symmetry with an incommensurate wavevector was observed, which is clearly visualized in the topographic image in Fig. 4c, with the corresponding Fourier transform image displaying distinct peaks denoted as $\mathbf{Q}_{exc}$ (Supplementary Note 7). By spatially mapping d*I*/d*V* on both the occupied side (−200 mV) and unoccupied side (100 mV) of the energy gap, we spectroscopically visualize the resulting superlattice modulations, demonstrating the spectroscopic contrast (Fig. 4c). The maxima (minima) of the local density of states at −200 mV correspond to the minima (maxima) of the local density

https://doi.org/10.1038/s41567-025-02917-6

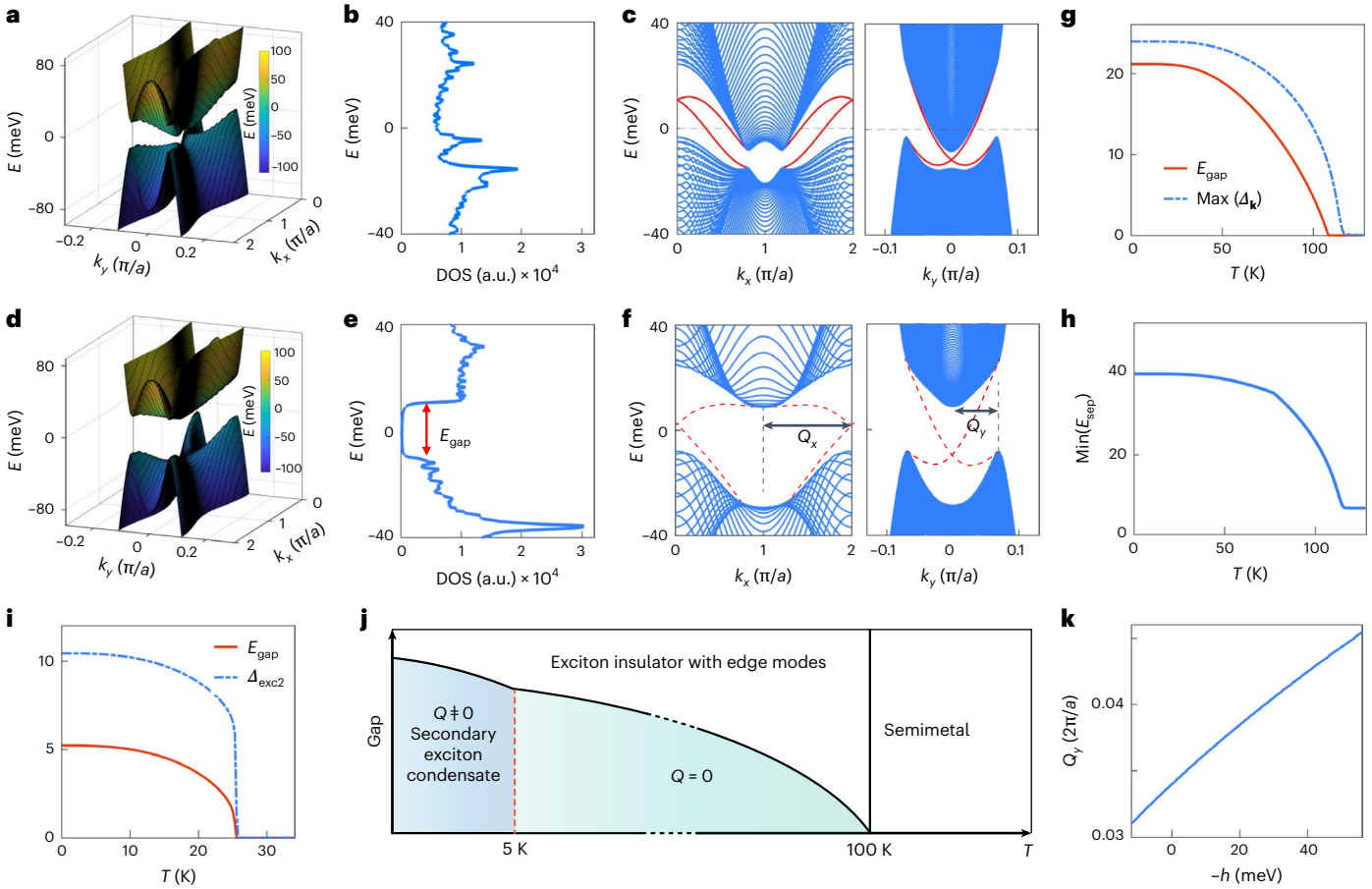

Fig. 5 | Theoretical modelling of the primary and secondary exciton condensation transitions. a, Low-energy band structure in the absence of an excitonic phase. **b**, Density of states in the absence of the excitonic phase. The system is metallic. The conduction band minimum is at 5.5 meV below the valence band maximum. **c**, Band structure for a ribbon with open boundaries along the y (left) and x directions (right). Blue bands represent the bulk continuum. Red curves illustrate the Z_2 topological edge states that connect the conduction and valence bands. **d**, Band structure in the presence of a primary excitonic order at $T = 10^{-3}$ K and $V = 1.16$ eV. **e**, Density of states in the presence of the primary excitonic order, exhibiting the opening of a fully developed bulk gap $E_{gap} \approx 21.5$ meV. **f**, Projection of the band structure along the x (left) and y (right) directions. Red dashed curves indicate the edge states. Q_x and Q_y denote the momentum separation between the conduction band minimum and valence band maximum along the k_x and k_y directions, respectively. **g**, Band energy gap E_{gap} (red curve) as a function of T, exhibiting a monotonic decrease with increasing T and its disappearance for $T \geq 110$ K, reminiscent of our experimental observation. The blue dashed curve plots the maximum value of the primary excitonic order parameter in momentum space $\max(\Delta_{\mathbf{k}})$ as a function of T. **h**, Minimum separation between the conduction and valence bands $\min(E_{sep})$ as a function of T. The separation is always finite on changing the temperature. **i**, Secondary finite-momentum excitonic order parameter Δ_{exc2} (blue dashed curve) and bulk energy gap E_{gap} (red curve) as functions of T, both developing below 25 K. We consider the same Coulomb interaction strength as that used for the primary excitons. The secondary excitonic order is substantially weaker than the primary one and exhibits a lower critical temperature. **j**, Schematic phase diagram of the discovered phases (presented using different shadings) of $Ta_2Pd_3Te_5$. **k**, Momentum separation Q_y between the valence band maximum and the Γ point as a function of the Zeeman-like energy h. DOS, density of states.

of states at 100 mV, indicating a reversal of the spectroscopic contrast. This is consistent with a translation-symmetry-breaking order. Moreover, the peaks of the wavevectors $\mathbf{Q}_{exc}$ obtained from the Fourier transform of the dI/dV maps coincide with those from the Fourier transform of the topography (Fig. 4c). Additionally, we investigated the energy dependence of the wavevectors $\mathbf{Q}_{exc}$ and found that they seem to be independent of energy, as the $\mathbf{Q}_{exc}$ peak locations remained non-dispersive outside the insulating gap (Fig. 4d). Within the insulating gap, by definition, no discernible spectroscopic signal was present. Notice that this secondary spontaneous electronic transition was accompanied by a marked increase in the spectral gap, as indicated in Fig. 1d by the traces collected at $T = 5$ and 4.2 K.

To understand the nature of the translation-symmetry-breaking order formed within the primary excitonic insulator state, we studied their dependence on the magnetic field (Fig. 4e,f and Extended Data Fig. 6). The series of topographic images acquired at various magnetic fields (0, 2, 4 and 6 T) at $T = 4.2$ K in Extended Data Fig. 6 clearly reveal the translation symmetry breaking under all fields. Interestingly, the corresponding wavevectors ($\mathbf{Q}_{exc}$) continuously changed with increasing magnetic field, as visualized by the Fourier transform of the topography. This field-induced evolution of $\mathbf{Q}_{exc}$ is further evidenced by the spectroscopic imaging presented in Fig. 4e, which reveals the spectroscopic contrast in real space in both the occupied and unoccupied sides of the energy gap. There is a contrast reversal between the two sides, akin to the zero-field data in Fig. 4c. Importantly, the $\mathbf{Q}_{exc}$ peaks obtained from the Fourier transforms of the dI/dV maps align with those obtained from the Fourier transform of the topography (Fig. 4e), both revealing markedly different $\mathbf{Q}_{exc}$ peak positions compared to the zero-field data. The field-induced evolution of $\mathbf{Q}_{exc}$, as summarized in Fig. 4f (also refer to Extended Data Fig. 6f), provides crucial insights into the nature of the ordering. At high temperatures (above $T \approx 100$ K), $Ta_2Pd_3Te_5$ is a semimetal with a negative indirect bandgap where particle- and hole-band extrema are separated by a finite, non-zero wavevector in the Brillouin zone. The primary exciton condensate is expected to inherit this characteristic wavevector in its effective (mean-field) band structure. The secondary order should then be

interpreted as another exciton condensate with this non-zero wavevector, which manifests as the periodicity of the excitonic superlattice modulation in real space. The magnetic field induces a continuous shift in the particle and hole bands due to the Zeeman effect, which in turn causes the wavevector of the secondary excitonic order to change continuously with increasing magnetic field. This behaviour was observed precisely in our experiments. Collectively, the experimental observations of an insulator-to-insulator transition (not driven by a structural instability), leading to the development of a translation-symmetry-breaking order (Supplementary Figs. 11–13), the lack of a Fermi surface in the parent state (Fig. 4) and the continuous magnetic field tunability of the **q** vector (Extended Data Fig. 6) strongly support the excitonic character of the secondary order[55]. Note that the edge states are still present in the secondary order (Supplementary Fig. 18). Furthermore, we substantiated the bulk nature of the excitonic order with systematic transport measurements (Supplementary Note 11 and Supplementary Fig. 12).

To theoretically understand both exciton condensation orders in $Ta_2Pd_3Te_5$, we formulated a two-band minimum model on a square lattice ('Determining the energy gap from the tunnelling spectra' in Methods and Supplementary Notes 12–14). With an appropriate choice of parameters, the model effectively mimics the low-energy band structure of monolayer $Ta_2Pd_3Te_5$ obtained through first-principles calculations (Extended Data Fig. 7). In its high-temperature phase, the system has no global gap, with the conduction band minimum situated near the M point ($\mathbf{k} = (0, \pi)$) and slightly below (by approximately 6 meV) the valence band maxima located along the $k_x = 0$ line (Fig. 5a). The model has an inverted band structure, which is consistent with the ARPES measurements. Owing to the gap between the two bands at all momenta, the inverted electronic band structure of $Ta_2Pd_3Te_5$ can be characterized by a Z_2 Kane–Mele topological invariant in the two-dimensional limit, which is non-trivial. The Z_2 invariant, under time-reversal and spin conservation symmetry (as present in our model), is determined by integrating the spin Berry curvature across the first Brillouin zone. Consequently, under open boundary conditions, this system has states at the edge that are buried by the bulk continuum (Fig. 5c).

To account for both excitonic instabilities, we incorporated a long-range Coulomb interaction and applied the Hartree–Fock mean-field approximation to the model. We initially identified that the primary excitonic order, which involves the pairing of electrons and holes with identical momentum, emerged at temperatures $T \leq 110$ K through a second-order phase transition as the temperature was decreased. This led to a substantial global bulk energy gap (Fig. 5d–f), which grew monotonically as the temperature was lowered (Fig. 5g). As the excitonic order strengthened, the direct gap between the conduction and valence bands was maintained (Fig. 5h). Consequently, the topological properties of the model were not changed by the primary excitonic order, which is evident in the persistence of the gapless edge states across the bulk insulating gap under open boundary conditions (Fig. 5f) and which is consistent with our experimental findings. Under the excitonic instability, the conduction band minimum and the valence band maxima remained well separated in momentum space. This separation triggers the formation of a secondary excitonic order, such that the ordering wavevector **Q** is equal to the momentum separation of the conduction band minimum and valence band maxima.

To model the secondary excitonic order, we used the same bare electronic structure and performed a self-consistent calculation to solve for the secondary excitonic order with finite momentum **Q**. This finite-momentum excitonic order primarily involves large momentum transfers mediated by the Coulomb interaction. As a result, for the same interaction strength as that for the primary order, it tended to be substantially weaker and exhibited a lower critical temperature ($T_{c2} \approx 25$ K), as shown in Fig. 5i. Moreover, as the temperature was decreased, the primary order first developed and opened the bulk gap, which suppressed the formation of the secondary order and further reduced T_{c2}. Therefore, although it breaks translation symmetry, this secondary order did not change the system topology (which is protected by time-reversal symmetry) and only minimally increased the bulk gap, in agreement with our experimental observations (Fig. 5j). We further accounted for the Zeeman coupling produced by externally applied magnetic fields in our calculations. We found that this Zeeman term can smoothly change the momentum separation between the conduction band minimum and valence band maxima (Fig. 5k), which is consistent with the change in the ordering wavevector under the application of a magnetic field.

This demonstration of a topological exciton insulator opens the door to investigating the intriguing interplay between non-trivial band topology and quantum many-body effects in a new context. Although the relationship between topology and electronic correlations has been intensely studied theoretically (for example, a Kane–Mele–Hubbard insulator), there are very few experimentally confirmed systems where electronic topology and correlations interplay, especially for itinerant systems displaying a full topological gap. They include the anomalous quantum Hall phases of moiré systems and topological Kondo insulators (for example, SmB_6)[56]. The topological excitonic insulator state in $Ta_2Pd_3Te_5$ now joins this rare group of correlated topological systems. The intertwined excitonic orders (Fig. 5j) and topological bands in $Ta_2Pd_3Te_5$ are unprecedented in other candidates for exciton insulators and invite integration into innovative optoelectronic and optical devices.

Online content

Any methods, additional references, Nature Portfolio reporting summaries, source data, extended data, supplementary information, acknowledgements, peer review information; details of author contributions and competing interests; and statements of data and code availability are available at https://doi.org/10.1038/s41567-025-02917-6.

References

1. Keldysh, L. & Kopaev, Y. Possible instability of semimetallic state toward Coulomb interaction. *Sov. Phys. Solid State* **6**, 2219–2224 (1964).
2. Cloizeaux, J. D. Exciton instability and crystallographic anomalies in semiconductors. *J. Phys. Chem. Solids* **26**, 259–266 (1965).
3. Jerome, D., Rice, T. M. & Kohn, W. Excitonic insulator. *Phys. Rev.* **158**, 462–475 (1967).
4. Halperin, B. I. & Rice, T. M. Possible anomalies at a semimetal–semiconductor transition. *Rev. Mod. Phys.* **40**, 755–766 (1968).
5. Snoke, D. Spontaneous Bose coherence of excitons and polaritons. *Science* **298**, 1368–1372 (2002).
6. Batista, C. D., Gubernatis, J. E., Bonča, J. & Lin, H. Q. Intermediate coupling theory of electronic ferroelectricity. *Phys. Rev. Lett.* **92**, 187601 (2004).
7. Mazza, G. & Georges, A. Superradiant quantum materials. *Phys. Rev. Lett.* **122**, 017401 (2019).
8. Safaei, S. & Mazziotti, D. A. Quantum signature of exciton condensation. *Phys. Rev. B* **98**, 045122 (2018).
9. Schouten, A. O., Sager-Smith, L. M. & Mazziotti, D. A. Large cumulant eigenvalue as a signature of exciton condensation. *Phys. Rev. B* **105**, 245151 (2022).
10. Baldini, E. et al. The spontaneous symmetry breaking in Ta_2NiSe_5 is structural in nature. *Proc. Natl Acad. Sci. USA* **120**, e2221688120 (2023).
11. Rohwer, T. et al. Collapse of long-range charge order tracked by time-resolved photoemission at high momenta. *Nature* **471**, 490–493 (2011).
12. Kogar, A. et al. Signatures of exciton condensation in a transition metal dichalcogenide. *Science* **358**, 1314–1317 (2017).
13. Lu, Y. F. et al. Zero-gap semiconductor to excitonic insulator transition in Ta_2NiSe_5. *Nat. Commun.* **8**, 14408 (2017).

14. Werdehausen, D. et al. Coherent order parameter oscillations in the ground state of the excitonic insulator Ta_2NiSe_5. *Sci. Adv.* **4**, eaap8652 (2018).
15. Varsano, D. et al. Carbon nanotubes as excitonic insulators. *Nat. Commun.* **8**, 1461 (2017).
16. Ataei, S. S., Varsano, D., Molinari, E. & Rontani, M. Evidence of ideal excitonic insulator in bulk MoS_2 under pressure. *Proc. Natl Acad. Sci. USA* **118**, e2010110118 (2021).
17. Mazza, G. et al. Nature of symmetry breaking at the excitonic insulator transition: Ta_2NiSe_5. *Phys. Rev. Lett.* **124**, 197601 (2020).
18. Subedi, A. et al. Orthorhombic-to-monoclinic transition in Ta_2NiSe_5 due to a zone-center optical phonon instability. *Phys. Rev. Mater.* **4**, 083601 (2020).
19. Watson, M. D. et al. Band hybridization at the semimetal-semiconductor transition of Ta_2NiSe_5 enabled by mirror-symmetry breaking. *Phys. Rev. Res.* **2**, 013236 (2020).
20. Eisenstein, J. P. & MacDonald, A. H. Bose–Einstein condensation of excitons in bilayer electron systems. *Nature* **432**, 691–694 (2004).
21. Nandi, D., Finck, A. D. K., Eisenstein, J. P., Pfeiffer, L. N. & West, K. W. Exciton condensation and perfect Coulomb drag. *Nature* **488**, 481–484 (2012).
22. Li, J. I. A., Taniguchi, T., Watanabe, K., Hone, J. & Dean, C. R. Excitonic superfluid phase in double bilayer graphene. *Nat. Phys.* **13**, 751–755 (2017).
23. Liu, X., Watanabe, K., Taniguchi, T., Halperin, B. I. & Kim, P. Quantum Hall drag of exciton condensate in graphene. *Nat. Phys.* **13**, 746–750 (2017).
24. Du, L. et al. Evidence for a topological excitonic insulator in InAs/GaSb bilayers. *Nat. Commun.* **8**, 1971 (2017).
25. Wang, R. et al. Excitonic topological order in imbalanced electron–hole bilayers. *Nature* **619**, 57–62 (2023).
26. Jia, Y. et al. Evidence for a monolayer excitonic insulator. *Nat. Phys.* **18**, 87–93 (2022).
27. Sun, B. et al. Evidence for equilibrium exciton condensation in monolayer WTe_2. *Nat. Phys.* **18**, 94–99 (2022).
28. Ali, M. et al. Large, non-saturating magnetoresistance in WTe_2. *Nature* **514**, 205–208 (2014).
29. Soluyanov, A. et al. Type-II Weyl semimetals. *Nature* **527**, 495–498 (2015).
30. Ma, X. et al. Ta_2NiSe_5: a candidate topological excitonic insulator with multiple band inversions. *Phys. Rev. B* **105**, 035138 (2022).
31. Wang, X. et al. Observation of topological edge states in the quantum spin Hall insulator $Ta_2Pd_3Te_5$. *Phys. Rev. B* **104**, L241408 (2021).
32. Wang, A. et al. A robust and tunable Luttinger liquid in correlated edge of transition-metal second-order topological insulator $Ta_2Pd_3Te_5$. *Nat. Commun.* **14**, 7647 (2023).
33. Fukutani, K. et al. Detecting photoelectrons from spontaneously formed excitons. *Nat. Phys.* **17**, 1024–1030 (2021).
34. Zhang, P. et al. Spontaneous gap opening and potential excitonic states in an ideal Dirac semimetal $Ta_2Pd_3Te_5$. *Phys. Rev. X* **14**, 011047 (2024).
35. Huang, J. et al. Evidence for an excitonic insulator state in $Ta_2Pd_3Te_5$. *Phys. Rev. X* **14**, 011046 (2024).
36. Yin, J.-X., Pan, S. H. & Hasan, M. Z. Probing topological quantum matter with scanning tunnelling microscopy. *Nat. Rev. Phys.* **3**, 249 (2021).
37. Yang, F. et al. Spatial and energy distribution of topological edge states in single Bi(111) bilayer. *Phys. Rev. Lett.* **109**, 016801 (2012).
38. Drozdov, I. K. et al. One-dimensional topological edge states of bismuth bilayers. *Nat. Phys.* **10**, 664–669 (2014).
39. Pauly, C. et al. Subnanometre-wide electron channels protected by topology. *Nat. Phys.* **11**, 338–343 (2015).
40. Wu, R. et al. Evidence for topological edge states in a large energy gap near the step edges on the surface of $ZrTe_5$. *Phys. Rev. X* **6**, 021017 (2016).
41. Li, X.-B. et al. Experimental observation of topological edge states at the surface step edge of the topological insulator $ZrTe_5$. *Phys. Rev. Lett.* **116**, 176803 (2016).
42. Wang, Z. et al. Topological edge states in a high-temperature superconductor FeSe/$SrTiO_3$(001) film. *Nat. Mater.* **15**, 968–973 (2016).
43. Sessi, P. et al. Robust spin-polarized midgap states at step edges of topological crystalline insulators. *Science* **354**, 1269–1273 (2016).
44. Peng, L. et al. Observation of topological states residing at step edges of WTe_2. *Nat. Commun.* **8**, 659 (2017).
45. Liu, S. et al. Experimental observation of conductive edge states in weak topological insulator candidate $HfTe_5$. *APL Mater.* **6**, 121111 (2018).
46. Ugeda, M. M. et al. Observation of topologically protected states at crystalline phase boundaries in single-layer WSe_2. *Nat. Commun.* **9**, 3401 (2018).
47. Liu, R. Z. et al. Experimental observations indicating the topological nature of the edge states on $HfTe_5$. *Chin. Phys. Lett.* **36**, 117301 (2019).
48. Shumiya, N. et al. Evidence of a room-temperature quantum spin Hall edge state in a higher-order topological insulator. *Nat. Mater.* **21**, 1111–1115 (2022).
49. Stühler, R. et al. Tomonaga–Luttinger liquid in the edge channels of a quantum spin Hall insulator. *Nat. Phys.* **16**, 47–51 (2020).
50. Shi, Y. et al. Imaging quantum spin Hall edges in monolayer WTe_2. *Sci. Adv.* **5**, eaat8799 (2019).
51. Dominguez, F. et al. Testing topological protection of edge states in hexagonal quantum spin Hall candidate materials. *Phys. Rev. B* **98**, 161407(R) (2018).
52. Fu, Y. S. et al. Observation of Zeeman effect in topological surface state with distinct material dependence. *Nat. Commun.* **7**, 10829 (2016).
53. Qi, X.-L. & Zhang, S.-C. Topological insulators and superconductors. *Rev. Mod. Phys.* **83**, 1057 (2011).
54. Bernevig, B. A. & Hughes, T. L. *Topological Insulators and Topological Superconductors* (Princeton Univ. Press, 2013).
55. Chen, C., Singh, B., Lin, H. & Pereira, V. M. Reproduction of the charge density wave phase diagram in 1T–$TiSe_2$ exposes its excitonic character. *Phys. Rev. Lett.* **121**, 226602 (2018).
56. Rachel, S. Interacting topological insulators: a review. *Rep. Prog. Phys.* **81**, 116501 (2018).

[1]Laboratory for Topological Quantum Matter and Advanced Spectroscopy, Department of Physics, Princeton University, Princeton, NJ, USA. [2]Hefei National Laboratory, Hefei, China. [3]Department of Physics, University of Zurich, Zurich, Switzerland. [4]Centre for Quantum Physics, Key Laboratory of Advanced Optoelectronic Quantum Architecture and Measurement (MOE), School of Physics, Beijing Institute of Technology, Beijing, China. [5]Beijing National Laboratory for Condensed Matter Physics and Institute of Physics, Chinese Academy of Sciences, Beijing, China. [6]Shenzhen Institute for Quantum Science and Engineering and Department of Physics, Southern University of Science and Technology (SUSTech), Shenzhen, China. [7]Quantum Science Center of Guangdong-Hong Kong-Macao Greater Bay Area (Guangdong), Shenzhen, China. [8]Shenzhen Key Laboratory of Quantum Science and Engineering, Shenzhen, China. [9]International Quantum Academy, Shenzhen, China. [10]International Center for Quantum Materials, School of Physics, Peking University, Beijing, China. [11]Princeton Materials Institute, Princeton University, Princeton, NJ, USA. [12]Institute for Quantum Matter and Department of Physics and Astronomy, Johns Hopkins University, Baltimore, MD, USA. [13]Advanced Light Source, Lawrence Berkeley National Laboratory, Berkeley, CA, USA. [14]ALBA Synchrotron Light Source, Cerdanyola del Vallès, Barcelona, Spain. [15]National Synchrotron Light Source II, Brookhaven National Laboratory, Upton, NY, USA. [16]Department of Physics, Technion – Israel Institute of Technology, Haifa, Israel. [17]The Helen Diller Quantum Center, Technion, Haifa, Israel. [18]Beijing Institute of Technology, Zhuhai, China. [19]National High Magnetic Field Laboratory, Tallahassee, FL, USA. [20]Department of Physics, Florida State University, Tallahassee, FL, USA. [21]Lawrence Berkeley National Laboratory, Berkeley, CA, USA. [22]Present address: Department of Materials Science and Engineering, University of California, Los Angeles, CA, USA. [23]These authors contributed equally: Md Shafayat Hossain, Zi-Jia Cheng, Yu-Xiao Jiang, Tyler A. Cochran, Song-Bo Zhang, Huangyu Wu. ✉e-mail: shossain@seas.ucla.edu; zhiweiwang@bit.edu.cn; mzhasan@princeton.edu

Methods

Single-crystal synthesis

$Ta_2Pd_3Te_5$ single crystals were synthesized using a flux method. A mixture of Ta powder (99.995% purity), Pd powder (99.95% purity) and Te chunks (99.99% purity) in a molar ratio of 2:4.5:7.5 was sealed in an evacuated quartz tube. All the manipulations were performed in an argon-filled glovebox to maintain an inert atmosphere. The sealed ampoule was then heated to 950 °C over 10 h and held at that temperature for 48 h to allow for crystal growth. Subsequently, the ampoule was gradually cooled to 800 °C with a ramp rate of 2 K h^{-1}. At this temperature, any excess liquid was removed through a centrifuging process. The resulting $Ta_2Pd_3Te_5$ single crystals obtained from the growth process were shiny and rod-like and had a silver-grey colour.

Scanning tunnelling microscopy

Single crystals were cleaved mechanically in situ at $T = 77$ K under ultra-high vacuum conditions ($<5 \times 10^{-10}$ mbar). Immediately after cleaving, the crystals were inserted into the microscope head, which was already at the ^{4}He base temperature (4.2 K). More than 20 single crystals were cleaved for this study. For each cleaved crystal, we explored surface areas over 10 μm × 10 μm looking for atomically flat surfaces. Topographic images were acquired in constant-current mode. Tunnelling conductance spectra were obtained with a commercial Ir/Pt tip (annealed under an ultra-high vacuum and then characterized with a reference sample) using standard lock-in amplifier techniques with a lock-in frequency of 977 Hz. The tunnelling junction set-ups used in the experiments are indicated in the corresponding figure captions. The magnetic field was applied through a zero-field cooling method. To acquire field-dependent tunnelling conductance measurements, the tip was first withdrawn from the sample, and then the magnetic field was slowly ramped to the desired value. The tip then re-approached the sample, and spectroscopic measurements were performed at the specific magnetic field. For temperature-dependent measurements, the tip was retracted from the sample, and the temperature was raised and stabilized for 12 h before the tip re-approached the sample for tunnelling measurements.

Scanning transmission electron microscopy

Thin lamellae were prepared by focused-ion-beam cutting. All samples for the experiments were polished using a 2-kV gallium ion beam to minimize damage to the surface caused by the high-energy ion beam. Transmission electron microscopy (TEM) imaging, atomic-resolution high-angle annular darkfield STEM imaging and atomic-level energy-dispersive X-ray spectroscopy mapping were performed using a Titan Cubed Themis 300 double Cs-corrected scanning/transmission electron microscope. The microscope was equipped with an extreme field emission gun source and operated at 300 kV. Additionally, a super-X energy-dispersive spectrometry system was used during the experiments.

X-ray diffraction measurements

Single-crystal X-ray diffraction measurements were performed using a custom-designed X-ray diffractometer equipped with a 17.48–keV X-ray source (Genix3D Mo Kα, Xenocs), which delivered 2.5×10^7 photons per second with a beam spot size of 150 μm at the sample position. The samples under investigation were mounted on a Huber four-circle diffractometer and cooled using a closed-cycle cryostat with a beryllium dome. The diffraction signals were captured by a highly sensitive, single-photon solid-state area detector (PILATUS3 R 1M), boasting 981 × 1,043 pixels, each with a size of 172 μm × 172 μm. During data acquisition, images were taken in 0.1° increments while we rotated the samples, and these images were subsequently converted into 3D mappings in momentum space. The crystallographic structure of the samples was confirmed to conform to the space group *Pnma*. The lattice parameters at room temperature were determined to be $a = 13.973$ Å, $b = 3.7098$ Å and $c = 18.564$ Å, with a measurement system error of 0.3%.

Angle-resolved photoemission spectroscopy

Synchrotron-based ARPES measurements were performed on single crystals cleaved in ultra-high vacuum ($<1 \times 10^{-10}$ mbar) on the ARPES manipulator. The high-resolution energy–momentum data shown in Fig. 2 and Supplementary Figs. 1–4 were collected at beamline 5–2 of the Stanford Synchrotron Radiation Lightsource in Stanford, United States. To avoid the non-reversible spectrum broadening due to degradation, all the temperature-dependent measurements were performed after cooling down a sample that was freshly cleaved at $T = 350$ K. The energy and momentum resolutions were better than 10 meV and 0.008 $Å^{-1}$. The preliminary data were taken at the beamline 4 of the Advanced Light Source in Berkeley, United States, the National Synchrotron Light Source in Brookhaven, United States, and LOREA of the ALBA Synchrotron light source in Barcelona, Spain.

First-principles calculations

Electronic band structure calculations were performed within density functional theory using the Vienna Ab initio Simulation Package (VASP)[57,58]. The general gradient approximation functional was used for treating the exchange-correlation effect[59]. The relativistic effect of spin–orbit coupling was included self-consistently in the calculations. An energy tolerance of 10^{-6} eV was used. We performed the calculations using 4 × 8 × 4 *k*-mesh centred at the Γ point for bulk, and 1 × 8 × 4 *k*-mesh for monolayer. We extracted the real-space tight-binding Hamiltonian with a Wannier function using the Wannier90 code[60] with *d*-orbitals of Ta and Pd and *p*-orbitals of Te as projections. The Wannier tight-binding Hamiltonian in the Wannier tools package[61] was used to study the topological properties.

Electrical transport measurements

To fabricate the $Ta_2Pd_3Te_5$ sample for transport measurements, we employed a polydimethylsiloxane stamp-based mechanical exfoliation technique. First, we patterned the sample contacts on the Si substrates with a 280-nm layer of thermal oxide using electron beam lithography, which was followed by chemical development and metal deposition (5 nm Cr/35 nm Au). The fresh $Ta_2Pd_3Te_5$ flakes were mechanically exfoliated from bulk single crystals on polydimethylsiloxane stamps. We carefully selected thick flakes (to capture the bulk properties of $Ta_2Pd_3Te_5$) with good geometry through optical microscopy. Next, we transferred the flakes onto the SiO_2/Si substrates that already had prepatterned Cr/Au electrodes. To preserve the intrinsic properties of the compound and minimize environmental effects, we encapsulated the samples using thin polymethyl methacrylate films with thicknesses around ~50 nm, which ensured that the samples on the devices were never directly exposed to air. All sample fabrication processes were performed in a glovebox equipped with a gas purification system (<1 ppm of O_2 and H_2O).

Electrical transport measurements were conducted using an Oxford Heliox system with a base temperature of 0.3 K and a maximum magnetic field up to 8 T. We employed a standard four-probe method to measure the resistance and differential resistance of the sample, using a lock-in amplifier technique with a lock-in frequency of 13 Hz. The reproducibility of the results was confirmed by conducting measurements in the National High Magnetic Field Laboratory in Tallahassee, Florida, United States. To ensure consistency, several devices were prepared and measured over several runs.

No detection of a structural instability in $Ta_2Pd_3Te_5$

As a structural instability can complicate the experimental detection of the transition to the excitonic insulator state, it was crucial that we investigated whether the observed excitonic insulator transition in $Ta_2Pd_3Te_5$ was accompanied by any structural instabilities.

For this purpose, we conducted a detailed structural analysis using TEM. Our STEM data revealed consistent atom arrangements compared to those of the pristine $Ta_2Pd_3Te_5$ crystal structure on different surfaces (Extended Data Figs. 1a,c and 2). Importantly, the selected-area electron diffraction patterns obtained from the lamellae cut with a focused ion beam at $T = 290$ and 90 K exhibited identical crystal lattices at both temperatures (Extended Data Fig. 1b,d). This observation indicates that the potential structural change associated with the excitonic transition at $T = 100$ K was below our detection threshold.

We conducted X-ray diffraction measurements at different temperatures (ranging from $T = 300$ to 20 K) to strengthen our conclusion regarding the structural changes in $Ta_2Pd_3Te_5$. The results are summarized in Extended Data Fig. 3. The data closely match the expected *Pnma* structure across the entire temperature range. The potential t-subgroups of space group 62 (*Pnma*) that are compatible with the mirror symmetry breaking in the zero-momentum excitonic insulator phase detected with our photoemission measurements are subgroups 19 ($P2_12_12_1$), 4 ($P2_1$), 2 (P-1) and 1 ($P1$). However, determining the exact subgroup will require future ultra-high-resolution structural measurements. We refer the reader to Supplementary Notes 8 and 9 and Supplementary Figs. 9 and 10 for more data and a discussion.

Determining the energy gap from the tunnelling spectra

In this section, we present the procedure that we used to determine the value of the spectroscopic energy gap from dI/dV curves. The key idea is to identify the edges of the energy gap, where a discernible non-zero dI/dV signal can be distinguished from the noisy zero dI/dV signal within the gap region[62]. The following steps outline our approach to determining the energy gap from a single dI/dV curve (Extended Data Fig. 4):

(1) Initially, we selected a bias range where the dI/dV signal takes the form: dI/d$V = 0 + \xi$, where 0 represents the mean dI/dV value within the spectroscopic gap and ξ represents the noise in the dI/dV signal. This was done for a bias voltage range $V \in [V_1, V_2]$, while avoiding the edges of the spectroscopic gap.
(2) Next, we calculated the standard deviation of the noisy dI/dV signal within the gap, denoted as $\sigma = \sqrt{\xi^2}$. By determining σ from the gap segment of the dI/dV curve, we established a noise floor for the dI/dV signal.
(3) We assumed a Gaussian distribution for ξ and defined $\Gamma = 2.36\sigma$, which represents the full-width at half-maximum. Two Gaussian signals can be distinguished if the difference between the means of the signals is greater than the full-width at half-maximum. Thus, we set Γ as the instrumental resolution of the dI/dV signal.
(4) A non-zero dI/dV signal could be detected only when dI/d$V > \Gamma$ within our instrumental resolution. We set Γ as the threshold value for identifying the edges of the energy gap.
(5) By solving the equation dI/d$V = \Gamma$, we determined the intersections V_a and V_b of the threshold value with the dI/dV spectroscopic curve. eV_a and eV_b represent the energies of the gap edge above and below E_F, respectively. Finally, we calculated $\Delta = eV_a - eV_b$ to obtain the value of the spectroscopic energy gap.

Broken symmetries due to the excitonic insulator transition

The excitons form due to the attractive Coulomb interaction between electron and hole states. This phenomenon is an electronic property related to the spontaneous breaking of particle–hole U(1) symmetry, akin to BCS superconductivity. In addition to U(1) symmetry, the excitonic order may also break the inversion and mirror symmetries.

In the absence of excitonic order, the conduction and valence bands at the Γ point have different parities, meaning that they are eigenstates of the inversion symmetry with different eigenvalues. The excitonic order hybridizes the conduction and valence bands, thereby violating this symmetry.

To elucidate this, we examined the symmetries of our model (see 'Determining the energy gap from the tunnelling spectra' in Methods for details of our model) both with and without the $Q = 0$ excitonic order. In the absence of excitonic order, the effective Hamiltonian is given by:

$$H(k_x, k_y) = h(k_x, k_y)\sigma_0 s_0 + \mathscr{M}(k_x, k_y)\sigma_z s_0 + A_x \sin k_x \sigma_x s_z + A_y \sin k_y \sigma_y s_0, \quad (1)$$

where $\{\sigma_x, \sigma_y, \sigma_z\}$ and σ_0 are the Pauli matrices and identity matrix for pseudo-spin $\{\alpha, \beta\}$, s_0 is the identity matrix, s_z is the third Pauli matrix for spin, A_x and A_y are model parameters, which can be obtained by fitting the model with density functional theory, and $h(k_x, k_y)$ and $\mathscr{M}(k_x, k_y)$ are even functions of k_x and k_y. This model exhibits inversion and mirror symmetries, as indicated by:

$$PH(k_x, k_y)P^{-1} = H(-k_x, -k_y), \quad (2a)$$

$$M_x H(k_x, k_y) M_x^{-1} = H(k_x, -k_y), \quad (2b)$$

$$M_y H(k_x, k_y) M_y^{-1} = H(-k_x, k_y), \quad (2c)$$

where $P = \sigma_z$, and $M_x = i\sigma_z s_x$ and $M_x = i\sigma_0 s_y$ are the inversion and mirror symmetry operators, respectively.

Applying the unitary transformation U, we can diagonalize the Hamiltonian as:

$$H' = UH(k_x, k_y)U^{-1} = E_c(k_x, k_y)(\sigma_0 + \sigma_z)s_0/2 + E_v(k_x, k_y)(\sigma_0 - \sigma_z)s_0/2, \quad (3)$$

where $E_c(k_x, k_y)$ and $E_v(k_x, k_y)$ are the conduction and valence bands. The transformation matrix is given by $U = U_1 \oplus U_2$, with

$$U_1 = (\cos(\phi/2), \sin(\phi/2)\, e^{i\theta}; -\sin(\phi/2)\, e^{-i\theta}, \cos(\phi/2)), \quad (4a)$$

$$U_2 = (\cos(\phi/2), -\sin(\phi/2)\, e^{-i\theta}; \sin(\phi/2)\, e^{i\theta}, \cos(\phi/2)), \quad (4b)$$

where φ and θ are determined by $\tan\phi = \sqrt{(A_x \sin k_x)^2 + (A_y \sin k_y)^2}/\mathscr{M}(k_x, k_y)$ and $e^{i\theta} = (A_x \sin k_x + iA_y \sin k_y)/\sqrt{(A_x \sin k_x)^2 + (A_y \sin k_y)^2}$.

Now, we consider the excitonic order. In the band basis, the exciton order parameter takes the form:

$$H'_{exc} = H' + \Delta(k_x, k_y)\sigma_x s_0. \quad (5)$$

Transforming back to the spin and orbital basis, the full Hamiltonian $H_{exc} = U^{-1}H'_{exc}U$ is given by

$$H_{exc}(k_x, k_y) = H(k_x, k_y) + \Delta(k_x, k_y)M, \quad (6)$$

where $M = M_1 \oplus M_2$ with

$$M_1 = (-\cos\theta \sin\phi, e^{i\theta}(\cos\theta\cos\phi - i\sin\theta); e^{-i\theta}(\cos\theta\cos\phi + i\sin\theta), \cos\theta\sin\phi), \quad (7a)$$

$$M_2 = (\cos\theta\sin\phi, e^{-i\theta}(\cos\theta\cos\phi + i\sin\theta); e^{i\theta}(\cos\theta\cos\phi - i\sin\theta), -\cos\theta\sin\phi). \quad (7b)$$

At the Gamma point, $M_1 = M_2 = (0, 1; 1, 0)$. We see that $H_{exc}(k_x, k_y)$ no longer obeys the symmetry relations in equation (2a)–(2c) due to the presence of the exciton term $\Delta(k_x, k_y)M$. This indicates that the inversion and mirror symmetries are explicitly broken.

Extended STM on the edge states

The existence of edge states in $Ta_2Pd_3Te_5$ was reported in a previous work[31,32]. In our study, presented in Fig. 3, we took an important step beyond the observation of the edge state by providing compelling evidence for its exponential localization and time-reversal-symmetry-protected Z_2 topological nature. In this section, we further support the data presented in Fig. 3 by providing extended results on the time-reversal-symmetry-protected nature of the edge state along different edge configurations. Extended Data Fig. 5 summarizes our STM measurements on two types of atomic step edges: (1) a monolayer step edge running along the *c* axis and perpendicular to the one-dimensional Te chains and (2) a four-atomic-layer-thick step edge along the *b* axis.

Extended Data Fig. 5a shows a monolayer atomic step edge along the *c* axis, identified through the topographic image and corresponding height profile. Notably, the spatially resolved d*I*/d*V* map at the Fermi energy, within the insulating bulk gap, reveals a pronounced edge state, akin to the step edge along the *b* axis shown in Fig. 3a. Energy-resolved d*I*/d*V* spectra on the step edge (Extended Data Fig. 5b) exhibit a substantial d*I*/d*V* signal (orange curves) around the Fermi energy, whereas the d*I*/d*V* spectrum away from the step edge (violet curves) has an insulating gap. Additionally, akin to the monolayer step edge along the *b* axis, the application of an external magnetic field perpendicular to the *b*–*c* plane leads to notable suppression of d*I*/d*V* measured at the step edge. The field-dependent tunnelling spectra, shown for $B = 0$, 2 and 4 T in Extended Data Fig. 5b, demonstrate the gradual opening of an insulating gap at the edge-state spectrum, confirming its time-reversal-symmetry-protected nature. The edge state and its time-reversal-symmetry-protected nature were also observed in multilayer step edges. For instance, we present the topography, the corresponding height profile and spectroscopic measurements of a four-atomic-layer-thick step edge in Extended Data Fig. 5c,d. The spectroscopic mapping reveals a pronounced gapless in-gap state at the Fermi energy at $B = 0$, whereas the tunnelling spectra at $B = 0$, 2 and 4 T exhibit the progressive opening of an energy gap with increasing magnetic field, highlighting the presence of a time-reversal-symmetry-protected topological edge state in the four-layer step edge.

Extended STM data on the field tunability of the secondary translation-symmetry-breaking excitonic order

Here, we present high-resolution topographic images obtained through STM that reveal the translation-symmetry-breaking ordering in $Ta_2Pd_3Te_5$. Extended Data Fig. 6a displays an atomically resolved topographic image of a pristine $Ta_2Pd_3Te_5$ (100) surface acquired at $T = 5$ K. The inset shows the corresponding Fourier transform image, indicating Bragg peaks along the *c* axis. Note that we are focusing on a small region in the Fourier transform image, and the Bragg peaks along the *b* axis are further away in **q** space (Fig. 1). At $T = 5$ K, no wavevector peaks were visible. However, when the sample was cooled to $T = 4.2$ K, then within the same region as in Extended Data Fig. 6a, we observed clear translation symmetry breaking in real space (Extended Data Fig. 6b). The corresponding Fourier transform image, plotted for the same range as the inset in Extended Data Fig. 6a, now exhibits distinct superlattice peaks labelled as $\mathbf{Q}_{exc}$.

Having observed the emergence of the translational-symmetry-breaking superlattice order at $T = 4.2$ K, we proceeded to investigate its magnetic field dependence. Extended Data Fig. 6c–e presents topographic images captured under magnetic fields of 2, 4 or 6 T, respectively. The topographic images clearly demonstrate the evolution of the superlattice modulation pattern as the magnetic field was changed. This evolution is further highlighted in the corresponding Fourier transform images, all plotted within the same **q** range, which illustrate the variation of $\mathbf{Q}_{exc}$ with increasing magnetic field. Notably, the positions of the Bragg peaks (Q_B) were unaffected by the magnetic field, as expected. To quantitatively summarize the change in $\mathbf{Q}_{exc}$ as a function of the magnetic field, Extended Data Fig. 6f displays a polar plot of the vector $\mathbf{Q}_{exc}$ at various magnetic field strengths (a scatter plot for $\mathbf{Q}_{exc}$ at different magnetic fields is shown in Fig. 4f). The plot clearly demonstrates the gradual evolution of $\mathbf{Q}_{exc}$ with increasing magnetic field, in accordance with the behaviour expected for a finite-momentum exciton condensate. This behaviour may arise due to the Zeeman effect experienced by the particle and hole bands associated with the exciton condensate upon the application of a magnetic field. The resulting Zeeman shift in the bands caused a change in the exciton wavevector, which in real space led to the variation of $\mathbf{Q}_{exc}$.

Discussion about the finite-momentum excitonic condensate

In semiconductors, the exciton energy typically shifts nearly linearly as a function of the magnetic field (Zeeman effect), which leads to an increase in the emission peak intensity[63,64]. However, the observed shift in the wavevector (Supplementary Fig. 12) of the excitonic phase in $Ta_2Pd_3Te_5$ was measured deep within the finite-**q** excitonic insulator state, which resembles an incommensurate charge density wave phase. Conventional charge density wave systems often display small Fermi surface pockets resulting from the opening of the associated gap and the resulting Brillouin-zone folding. Small Fermi surface sheets are highly susceptible to Landau quantization and the Zeeman effect, being deformed by the latter to accommodate an integer number of magnetic flux quanta. As the magnetic field increases, the nesting vector is understood to shift in *k*-space to minimize the free energy of the system to maintain the stability of the charge density wave. In $Ta_2Pd_3Te_5$, the finite-momentum excitons below $T = 5$ K emerge from a fully gapped state without a Fermi surface (d*I*/d*V* spectra in Fig. 1d). Thus, the mechanism leading to the shift in the modulation vector of the finite-**q** excitons in $Ta_2Pd_3Te_5$ probably differs from that of conventional charge density waves. Although we did not detect any evidence for a structural transition at $T = 5$ K with STM, which has angstrom-scale resolution (Supplementary Fig. 8), we cannot discard a more subtle structural change that could be revealed by high-resolution X-ray diffraction measurements at low temperatures. However, these are beyond our experimental capabilities and should motivate future studies. Importantly, the absence of a density of states at the Fermi level above the transition observed at $T = 5$ K (Fig. 1d) rules out conventional scenarios such as a charge density wave ground state. The field tuning of the **q** vector would, therefore, mark the direct experimental demonstration of **q**-vector tuning of an excitonic insulating state by a magnetic field.

Furthermore, we substantiated the bulk nature of the excitonic order with systematic transport experiments. The results of these experiments (Supplementary Fig. 12) support the overall STM observations as well as the related conclusions. We observed clear electric threshold fields E_{th} for nonlinear carrier conduction due to the sliding or phason mode of the translation-symmetry-breaking excitonic order[65], but only below $T \approx 5$ K. Satellite peaks, associated with the finite-momentum exciton condensate, become observable in the Fourier transform of the STM images precisely in this range of temperatures. The absence of both translation symmetry breaking in STM images and nonlinear electrical conduction confirms the absence of a translation-symmetry-breaking order and the zero-momentum nature of the electron–hole condensate observed above $T \approx 5$ K. Furthermore, E_{th} continuously changes with the magnetic field, in agreement with our STM results (see Supplementary Note 11 for details). The two excitonic transitions also appear in the thermodynamic measurements (Supplementary Note 10 and Supplementary Fig. 11), clearly indicating the bulk nature of the excitonic transitions.

Theoretical description of the two excitonic instabilities in $Ta_2Pd_3Te_5$

In our experiments, the edge states were gapless in the absence of magnetic fields. This observation indicates the presence of time-reversal

symmetry, which prevented the coupling between the two spin species. This allowed us to address the two spin species separately. Therefore, we focused on one spin species to elucidate the essential physics, whereas the results for the other spin species could be straightforwardly obtained by exploiting time-reversal symmetry. The low-energy band structure for monolayer $Ta_2Pd_3Te_5$, derived from first-principles calculations, is displayed in Extended Data Fig. 7. The conduction band minimum was at $\mathbf{k} = (0, \pi/c)$, whereas the valence band maxima were close to the $k_y = 0$ line. Notably, the system was gapless in the absence of the excitonic order. Specifically, the bottom of the conduction band minimum was slightly lower (by 6 meV) with respect to the top of the valence band maxima. Moreover, the band structure was topological and could be characterized by a non-zero topological invariant. Based on these properties, we constructed a two-band minimum model on a square lattice as follows:

$$H = \sum_{\mathbf{k}} \Psi_{\mathbf{k}}^{\dagger}\{\mathcal{M}(\mathbf{k})\sigma_z + A_x \sin k_x \sigma_x + A_y \sin k_y \sigma_y + h(\mathbf{k})\sigma_0\}\Psi_{\mathbf{k}}. \tag{8}$$

In equation (8), $\Psi_{\mathbf{k}} = (c_{\alpha,\mathbf{k}}, c_{\beta,\mathbf{k}})^{\mathrm{T}}$, $\mathcal{M}(\mathbf{k}) = M_0 + M_x(1-\cos k_x) + M_y(1-\cos k_y)$ and $h(\mathbf{k}) = C_x(1+\cos k_x) + C_y(1-\cos k_y)$. The lattice constants were set to unity. This is, essentially, a modified Bernevig–Hughes–Zhang model[66].

The two energy bands are given by:

$$\varepsilon_{c/v}(\mathbf{k}) = h(\mathbf{k}) \pm E(\mathbf{k}), \tag{9}$$

where $E(\mathbf{k}) = [\mathcal{M}(\mathbf{k})^2 + A_x^2 \sin^2 k_x + A_y^2 \sin^2 k_y]^{1/2}$. To mimic the low-energy band structure of monolayer $Ta_2Pd_3Te_5$, we chose the following parameter values: $M_0 = -0.072$ eV, $M_y = 3.2$ eV, $M_x = 0.04$ eV, $A_x = 0.006$ eV, $A_y = 0.064$ eV, $C_x = 0.003$ eV and $C_y = -0.24$ eV. The resulting band structure is illustrated in Fig. 5a. The conduction band minimum was slightly lower (by 5.5 meV) with respect to the valence band maxima. As dictated by the non-trivial topological invariant, the model exhibits gapless edge states under open boundaries. However, the edge states are buried by the bulk continuum (Fig. 5c).

Topological excitonic instability. We considered the Coulomb interaction, which can be expressed in momentum space as[67]:

$$H_{\mathrm{int}} = \frac{1}{N}\sum_{\mathbf{k},\mathbf{k}',\mathbf{q}} W(\mathbf{q}) c_{\mathbf{k}+\mathbf{q},c}^{\dagger} c_{\mathbf{k}'-\mathbf{q},v}^{\dagger} c_{\mathbf{k}',v} c_{\mathbf{k},c}, \tag{10}$$

where $c_{\mathbf{k},c(v)}^{\dagger}$ and $c_{\mathbf{k},c(v)}$ represent creation and annihilation operators for an electron with momentum $\mathbf{k}$ at the conduction (valence) band, respectively. N is the number of k points in the Brillouin zone. $W(\mathbf{q})$ stands for the $\mathbf{q}$-resolved screened Coulomb interaction:

$$W(\mathbf{q}) = \frac{U(\mathbf{q})}{1 + 2\pi\alpha|\mathbf{q}|}, \tag{11}$$

and $U(\mathbf{q}) = V/|\mathbf{q}|$ denotes the unscreened Coulomb interaction, which is the dominant contribution to the electron–hole attraction. We consider two-dimensional screening, which leads to an intrinsic $\mathbf{q}$-dependent dielectric function of the form $1/(1 + 2\pi\alpha|\mathbf{q}|)$, as shown in equation (11)[68,69]. V represents the interaction strength, and α parametrizes the screening strength. In the Coulomb interaction described by equation (10), the summation involves three momenta, $\mathbf{k}$, $\mathbf{k}'$ and $\mathbf{q}$. To simplify this for the Hartree–Fock approximation, we imposed specific constraints on the relation between these momenta, guided by the electronic band structure of the material. Specifically, we considered $\mathbf{q} = \mathbf{k}' - \mathbf{k}$ and $\mathbf{q} = \mathbf{k}' - \mathbf{k} \pm \mathbf{Q}$ in equation (1), where $\mathbf{Q}$ is the ordering wavevector (corresponding to the distance between the positions of the conduction minimum and valence maximum). Consequently, the Coulomb interaction can be rewritten as two terms (components):

$$\begin{aligned} H_{\mathrm{int}} = &\frac{1}{N}\textstyle\sum_{\mathbf{k},\mathbf{k}'} W(\mathbf{k}'-\mathbf{k}) c_{\mathbf{k}',c}^{\dagger} c_{\mathbf{k},v}^{\dagger} c_{\mathbf{k}',v} c_{\mathbf{k},c} \\ &+\frac{1}{N}\textstyle\sum_{\mathbf{k},\mathbf{k}'} W(\mathbf{k}'-\mathbf{k}\pm\mathbf{Q}) c_{\mathbf{k}'\mp\mathbf{Q},c}^{\dagger} c_{\mathbf{k}\pm\mathbf{Q},v}^{\dagger} c_{\mathbf{k}',v} c_{\mathbf{k},c}. \end{aligned} \tag{12}$$

Note that the two terms arise from different restrictions of $\mathbf{q}$ in equation (1) and, therefore, are independent. With these restrictions, the summation now involves only two momenta $\mathbf{k}$ and $\mathbf{k}'$, enabling us to perform the Hartree–Fock decomposition.

We first focus on the first term Q_y in equation (12) and decouple it as

$$H_{\mathrm{exc}} = \begin{pmatrix} 0 & \Delta_{\mathbf{k}} \\ \Delta_{\mathbf{k}} & 0 \end{pmatrix} \tag{13}$$

in the band basis $(c_{\mathbf{k},c}, c_{\mathbf{k},v})$. The momentum-dependent order parameter $\Delta_{\mathbf{k}}$ is calculated self-consistently through

$$\Delta_{\mathbf{k}} = -\frac{1}{N}\sum_{\mathbf{k}'} W(\mathbf{k}-\mathbf{k}') \left\langle c_{\mathbf{k}',c}^{\dagger} c_{\mathbf{k}',v} \right\rangle, \tag{14}$$

where $\langle \ldots \rangle$ stands for the quantum statistic average. This yields the primary excitonic order that couples electrons and holes with identical momenta $\mathbf{k}$. Importantly, the order parameter is influenced solely by the Fock term. The influence of the Hartree term is detailed in Supplementary Note 14.

Through a self-consistent computation, using an interaction strength $V = 1.16$ eV, a small screening factor $\alpha = 0.3$ (in units of the lattice constant) and employing a 201×561 grid within the Brillouin zone, we observed the distinctive emergence of the excitonic order. This order engendered a bandgap for temperatures $T < T_c \approx 110$ K. The order parameter $\Delta_{\mathbf{k}}$ was most pronounced near the k_x axis ($k_y = 0$), where the two bands were closest to each other. With decreasing T, $\Delta_{\mathbf{k}}$ became stronger, which resulted in a consistent increase in the bulk gap. Ultimately, for $T \leq 30$ K, the bulk gap saturated at a large value of 21.5 meV. Notably, the valence maxima relocated to $\pm(0, 0.071\pi)$ (as depicted in Fig. 5d).

Figure 5g shows the calculated maximum value of the order parameter $\max(\Delta_{\mathbf{k}})$ as a function of T. We found that the critical temperature for $\Delta_{\mathbf{k}}$ was $T_c' \approx 120$ K, which substantially exceeded T_c. This deviation was due to the negative bandgap in the bare band structure (without $\Delta_{\mathbf{k}}$). Additionally, Fig. 5h portrays the minimum value of the energy separation between the conduction and valence bands, $\min(E_{\mathrm{sep}})$, as a function of T. Notably, ΔE_{min} remained consistently positive throughout the entire range of T. This observation indicates that, when we turned on the excitonic order by decreasing temperature, the two bands still did not touch each other. Thus, the topology of the system was preserved.

Note that in refs. 70,71, exciton condensation in the Bernevig–Hughes–Zhang model was studied under the assumption of local interaction. It was shown that the interaction spontaneously breaks the time-reversal, spin U(1) and parity symmetries, eventually driving the system into a trivial band insulator. However, this cannot explain our experiments, as we observed gapless edge modes that became more robust and localized within the exciton phase.

Excitonic translation-symmetry-breaking order. Next, we consider the second term in the Coulomb interaction, equation (12), which involves the ordering wavevector $\mathbf{Q} \approx (\pi, 0.035\pi)$. This allows the coupling between the conduction band minimum and valence band maxima. In the Hartree–Fock decomposition, a finite-momentum excitonic order is found:

$$\Delta_{\mathrm{exc2}} = -\frac{1}{N}\sum_{\mathbf{k}'} W(\mathbf{k}-\mathbf{k}'\pm\mathbf{Q}) \left\langle c_{\mathbf{k}'\mp\mathbf{Q},c}^{\dagger} c_{\mathbf{k}',v} \right\rangle. \tag{15}$$

This order couples electrons and holes with a finite momentum difference $\pm\mathbf{Q}$. In the calculation, we split the Brillouin zone into small

rectangular pieces with an area of Q_xQ_y and considered eight pieces with the lowest energies. For simplicity, we assumed an approximately constant interaction strength, $U_{CDW} = W(\mathbf{Q})$, between the conduction and valence bands, originating from the next-nearest-neighbour pieces in momentum space. We used the same values, $V = 1.16$ eV and $\alpha = 0.3$, used for the primary excitons. Note that the wavevector for the translation-symmetry-breaking ordering is not necessarily commensurate. The results are the same if more pieces of the Brillouin zone are considered, because the finite-momentum excitonic order occurs only between the pieces that are closest to the bandgap. Figure 5i shows the calculated finite-momentum excitonic order parameter Δ_{exc2} (blue dashed curve) and bulk energy gap E_{gap} (red curve) as functions of T. A secondary excitonic order developed, but it was substantially weaker than the primary one and had a lower critical temperature ($T_{c2} \approx 25$ K). It is also important to note that as the temperature decreased, the primary excitonic order developed first, opening a global bulk gap. This bulk gap made it harder for the second finite-momentum excitonic order to form, thereby further lowering T_{c2}.

Note that the Coulomb interaction can, in principle, generate an infinite number of orders, each associated with a given $\mathbf{q}$. Based on the unique band structure and experimental observations, we considered two of these orders that are the most prominent and relevant to the experiments. The first one corresponds to the $\mathbf{q} = \mathbf{k} - \mathbf{k}'$ component of the Coulomb interaction, resulting in a $Q = 0$ excitonic order. The second order, corresponding to $\mathbf{q} = \mathbf{k} - \mathbf{k}' + \mathbf{Q}$, resulted in a $Q \neq 0$ excitonic order. Importantly, the second effect fundamentally differs from, and is not included in, the first, even though both are rooted in the same Coulomb interaction.

Magnetic field dependence. Here we investigate the influence of the magnetic field on the wavevector of the translation-symmetry-breaking order, based on the Zeeman coupling. As previously discussed, the wavevector can be determined by the momentum separation $\mathbf{Q}$ of the conduction band minimum and valence band maxima in momentum space. In the model, the magnetic field B can be incorporated through a Zeeman-like term:

$$H_{Zeeman} = h\sigma_z. \tag{16}$$

Here $h = \tilde{g}\mu_B B$ represents the Zeeman energy, where $\tilde{g}$ is the effective g-factor difference between two orbitals (which form the pseudo-spin $\{\alpha, \beta\}$ degrees of freedom in equation (8)) and μ_B is the Bohr magneton. As shown before, the conduction band minimum is always at the M point, and the x component of $\mathbf{Q}$ remains relatively fixed at π, particularly in the presence of the primary excitonic order. Thus, it suffices to focus solely on the y component of the wavevector of the translation-symmetry-breaking order. The problem can then be reformulated to investigate how h influences the y component of the momentum separation (Q_y). Its solution is illustrated by Fig. 5k.

The impact of magnetic fields on the band structure is complex, as it encompasses both Zeeman and orbital effects. In general, distinct orbitals generally respond differently to an applied magnetic field due to their distinct angular momenta. To simplify and illustrate the key physics, we modelled this response using an effective g-factor between the two orbitals, resulting in a Zeeman-like term in equation (16).

In general, the magnetic field couples to the system in two key ways:

(1) Orbital coupling, which leads to the formation of Landau levels.
(2) Zeeman coupling, which affects the spin and orbital magnetic moments and is encapsulated by the effective g-factor.

Zeeman coupling (effect 2) reduces the excitonic insulator gap, whereas orbital coupling (effect 1) generally increases the exciton binding energy, at least in simple models[72,73]. In the excitonic insulator phase—where excitons have already condensed—a larger binding energy may lead to a larger gap, analogous to superconductors. Because this gap is induced by correlation, its enhancement is governed not only by the cyclotron frequency but also by the Coulomb interaction strength. This effect can outweigh the Zeeman contribution, resulting in an increase in the energy gap with the magnetic field, as observed in our experiments, rather than the expected Zeeman-driven suppression.

Quantifying these competing effects poses different challenges. Estimating the orbital coupling effect required a robust tight-binding model derived from density functional theory followed by a mean-field exciton calculation. However, due to technical difficulties in converging hybrid functional calculations for this material, we leave a quantitative prediction of the exciton gap evolution under a magnetic field for future work.

On the other hand, estimating the effective g-factor is more feasible—at least for the bare band structure derived from a monolayer calculation. Using the method in ref. 74, we obtained g-factors of $g \approx 2$ for in-plane and $g \approx 2.8$ for out-of-plane magnetic fields. This resulted in a Zeeman-induced gap reduction of $E_z = g\mu_B B \approx 1$ meV at 6 T (out-of-plane), which is substantiallysmaller than the 6 meV gap change observed experimentally. We, therefore, attributed the dominant effect to orbital coupling. Although Zeeman coupling was undoubtedly present, its influence was quantitatively overshadowed by orbital effects. Future theoretical studies will be necessary to fully unravel the interplay between the orbital and Zeeman contributions to the excitonic insulator gap.

Finally, it is important to emphasize that, from a broad perspective, the excitonic insulator is expected to endure high magnetic fields due to the absence of a Meissner effect (intrinsic to superconductors). Fenton[75] investigated the field dependence of the excitonic insulator based on orbital coupling, demonstrating that in systems with a band overlap (such as $Ta_2Pd_3Te_5$), or in small-bandgap semiconductors, the application of a magnetic field induces a stronger excitonic insulator than observed with no field. Note that ref. 75 assumed isotropic bands, thus implying that there was no anticipated shift in the wavevector. In a more complete consideration, the combination of orbital and Zeeman effects and also Fermi surface anisotropies need to be considered. In materials featuring anisotropic bands, like $Ta_2Pd_3Te_5$, this would generically also lead to a shift in the wavevector of the excitonic order under applied magnetic fields, particularly if the initial state was incommensurate. These basic trends—the magnetic field enhancement of the exciton gap as well as a shift of the ordering wavevector—are fully consistent with our experimental observations.

Data availability

Source data are provided with this paper. Further data are available from the corresponding authors upon request.

References

57. Hohenberg, P. & Kohn, W. Inhomogeneous electron gas. *Phys. Rev.* **136**, B864 (1964).
58. Kresse, G. & Furthmüller, J. Efficient iterative schemes for ab initio total-energy calculations using a plane-wave basis set. *Phys. Rev. B* **54**, 11169 (1996).
59. Perdew, J. P., Burke, K. & Ernzerhof, M. Generalized gradient approximation made simple. *Phys. Rev. Lett.* **77**, 3865 (1996).
60. Mostofi, A. et al. Wannier90: a tool for obtaining maximally-localised Wannier functions. *Comput. Phys. Commun.* **178**, 685 (2008).
61. Wu, Q., Zhang, S., Song, H.-F., Troyer, M. & Soluyanov, A. A. WannierTools: an open-source software package for novel topological materials. *Comput. Phys. Commun.* **224**, 405 (2018).
62. Lee, I. et al. Imaging Dirac-mass disorder from magnetic dopant atoms in the ferromagnetic topological insulator $Cr_x(Bi_{0.1}Sb_{0.9})_{2-x}Te_3$. *Proc. Natl Acad. Sci. USA* **112**, 1316–1321 (2014).
63. Edelstein, W. et al. Two-dimensional excitons in magnetic fields. *Phys. Rev. B* **39**, 7697 (1989).

64. Stier, A. et al. Exciton diamagnetic shifts and valley Zeeman effects in monolayer WS_2 and MoS_2 to 65 tesla. *Nat. Commun.* **7**, 10643 (2016).
65. Grüner, G. The dynamics of charge-density waves. *Rev. Mod. Phys.* **60**, 1129–1181 (1988).
66. Bernevig, B. A., Hughes, T. L. & Shou-Cheng Zhang, S.-C. Quantum spin Hall effect and topological phase transition in HgTe quantum wells. *Science* **314**, 1757–1761 (2006).
67. Gao, Q. et al. Evidence of high-temperature exciton condensation in a two-dimensional semimetal. *Nat. Commun.* **14**, 994 (2023).
68. Cudazzo, P., Tokatly, I. V. & Rubio, A. Dielectric screening in two-dimensional insulators: implications for excitonic and impurity states in graphene. *Phys. Rev. B* **84**, 085406 (2011).
69. Varsano, D., Palummo, M., Molinari, E. & Rontani, M. A monolayer transition-metal dichalcogenide as a topological excitonic insulator. *Nat. Nanotechnol.* **15**, 367 (2020).
70. Amaricci, A., Mazza, G., Capone, M. & Fabrizio, M. Exciton condensation in strongly correlated quantum spin Hall insulators. *Phys. Rev. B* **107**, 115117 (2023).
71. Blason, A. & Fabrizio, M. Exciton topology and condensation in a model quantum spin Hall insulator. *Phys. Rev. B* **102**, 035146 (2020).
72. Cong, K., Noe, G. T. & Kono, J. in *Encyclopedia of Modern Optics* 2nd edn (eds Guenther, B. D. & Steel, D.) 63–81 (Elsevier, 2018).
73. Jahan, K. L. et al. Magnetic field effect on the energy levels of an exciton in a GaAs quantum dot: application for excitonic lasers. *Sci. Rep.* **8**, 5073 (2018).
74. Förste, J. et al. Exciton *g*-factors in monolayer and bilayer WSe_2 from experiment and theory. *Nat. Commun.* **11**, 4539 (2020).
75. Fenton, E. W. Excitonic insulator in a magnetic field. *Phys. Rev.* **170**, 816 (1968).

Acknowledgements

M.Z.H.'s group at Princeton University acknowledges primary support from the US Department of Energy (DOE), Office of Science, under the Basic Energy Sciences (DOE-BES) programme (grant no. DOE/BES DE-FG-02- 05ER46200), for the advanced spectroscopic measurements and theoretical including ARPES, and the National Quantum Information Science Research Centers, the Quantum Science Center and Princeton University; ARPES, STM and transport instrumentation support from the Gordon and Betty Moore Foundation (grant no. GBMF9461) and Princeton University; and support from the US DOE under the Basic Energy Sciences (DOE-BES) programme (grant no. DOE/BES DE-FG-02- 05ER46200) for the theoretical work and extensive sample characterization. This research utilized the Stanford Synchrotron Radiation Lightsource (SSRL) at SLAC National Accelerator Laboratory, supported by the US DOE, Office of Science, Office of Basic Energy Sciences under contract no. DE-AC02-76SF00515. It also used Beamline 21-ID-1 (ESM-ARPES) at the National Synchrotron Light Source II (NSLS-II), a DOE Office of Science User Facility operated by Brookhaven National Laboratory under Contract No. DE-SC0012704. Additional support was provided by the Advanced Light Source (ALS), a DOE Office of Science User Facility operated under contract no. DE-AC02-05CH11231. We acknowledge D. Lu and M. Hashimoto for their expert support at Beamline 5-2 of SSRL, SLAC National Accelerator Laboratory, and E. Vescovo and T. Yilmaz for their technical assistance at Beamline 21-ID-1 (ESM-ARPES) of NSLS-II. We also thank C. Jozwiak, A. Bostwick and E. Rotenberg for their support at Beamline 7.0.2 of the ALS. Crystal growth at Beijing Institute of Technology is supported by the National Key Research and Development Program of China (grant nos. 2020YFA0308800 and 2022YFA1403400), the National Science Foundation of China (grant no. 92065109), the Beijing Natural Science Foundation (grant no. Z210006) and the Beijing National Laboratory for Condensed Matter Physics (grant no. 2023BNLCMPKF007). L.B. is supported by DOE-BES (award no. DE-SC0002613). The National High Magnetic Field Laboratory acknowledges support from a US NSF cooperative agreement (grant no. DMR-DMR-2128556) and the state of Florida. We thank T. Murphy, G. Jones, L. Jiao and R. Nowell at the National High Magnetic Field Laboratory for technical support. T.N. acknowledges support from the Swiss National Science Foundation through a Consolidator Grant (iTQC, TMCG-2_213805). Z.W. thanks the Analysis and Testing Center at BIT for assistance with facility support. Y.Y.P. is grateful for financial support from the National Natural Science Foundation of China (grant no. 11974029). G.C. and N.Y. acknowledge the use of Princeton's Imaging and Analysis Center, which is partially supported by the Princeton Center for Complex Materials, a National Science Foundation (NSF)-MRSEC programme (DMR-2011750). This research used resources of the Advanced Light Source, which is a DOE Office of Science User Facility (contract no. DE-AC02-05CH11231). S.-B.Z. is supported by the start-up fund at HFNL, the Innovation Program for Quantum Science and Technology (grant no. 2021ZD0302800) and the Anhui Initiative in Quantum Information Technologies (grant no. AHY170000).

Author contributions

M.S.H. conceived the project. The STM experiments were performed by M.S.H. and Y.-X.J. Transport experiments were performed by M.S.H. and Q.Z. under consultation with L.B. The ARPES experiments were performed by Z.-J.C., T.A.C. and B.K. with the help of J.D.D., M.T., J.D., E.V. and A.R. S.-B.Z. performed the tight-binding calculations under consultation with T.N. X.L. performed the first-principles calculations under consultation with T.N. The crystals were grown by H.W., J.L., Y.Y. and Z.W. G.C. and N.Y. performed the TEM. X.Z. and Y.P. performed X-ray measurements. M.L., X.P.Y., J.Z. and J.-X.Y. helped with the measurements. A.K. helped with interpreting the data. M.S.H., Z.-J.C., T.A.C., T.N., L.B. and M.Z.H. developed the figures and wrote the paper. M.Z.H. supervised the project. All authors discussed and interpreted the results and participated in drawing the conclusions.

Competing interests

The authors declare no competing interests.

Additional information

Extended data is available for this paper at https://doi.org/10.1038/s41567-025-02917-6.

Supplementary information The online version contains supplementary material available at https://doi.org/10.1038/s41567-025-02917-6.

Correspondence and requests for materials should be addressed to Md Shafayat Hossain, Zhiwei Wang or M. Zahid Hasan.

Peer review information *Nature Physics* thanks the anonymous reviewers for their contribution to the peer review of this work.

https://doi.org/10.1038/s41567-025-02917-6

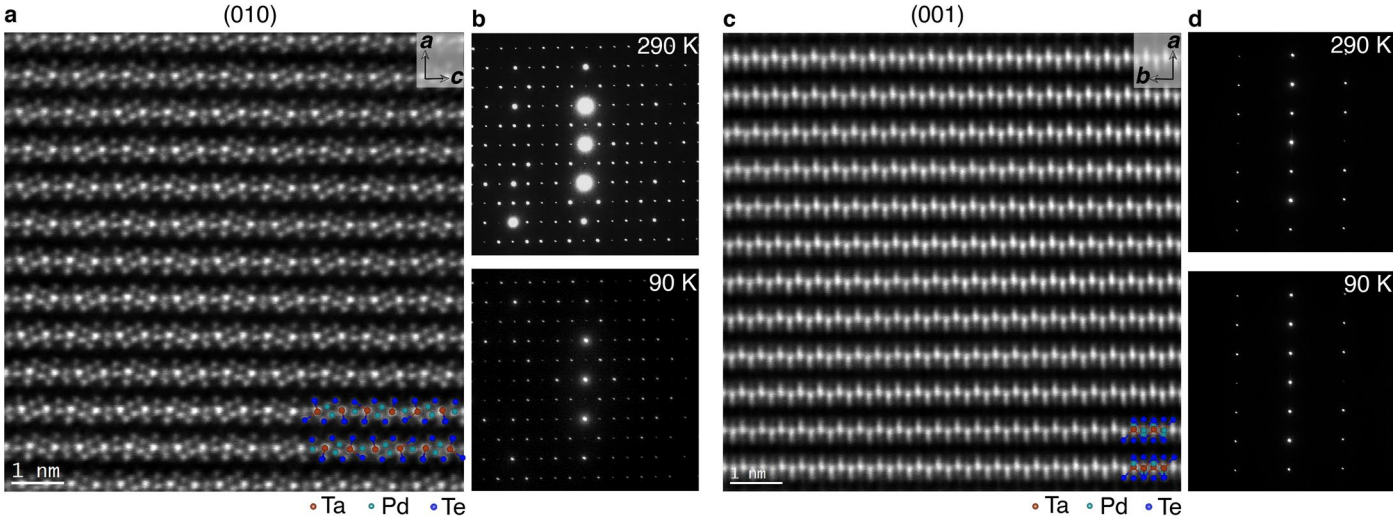

Extended Data Fig. 1 | Selected area electron diffraction patterns detecting no lattice instabilities near $T = 100$ K. a, Atomic-resolution image of the (010) surface of a lamella captured by scanning transmission electron microscopy, demonstrating a consistent atomic arrangement when compared to pristine $Ta_2Pd_3Te_5$ (010) crystallographic structure. **b**, Selected area electron diffraction patterns obtained from the focused-ion-beam cut lamella at $T = 290$ K (top) and 90 K (bottom). The patterns exhibit identical crystal lattice at both temperatures, detecting no structural phase change in this temperature range. **c**, Atomic-resolution scanning transmission electron microscopy image of the (001) surface, revealing a consistent atom arrangement when compared to pristine $Ta_2Pd_3Te_5$ (001). **d**, Selected area electron diffraction patterns acquired from the focused-ion-beam cut lamella at $T = 290$ K (top) and 90 K (bottom). Akin to panel **b**, the patterns demonstrate the same crystal lattice at both temperatures. The temperature-dependent selected area electron diffraction patterns detect no structural phase transition around 100 K.

https://doi.org/10.1038/s41567-025-02917-6

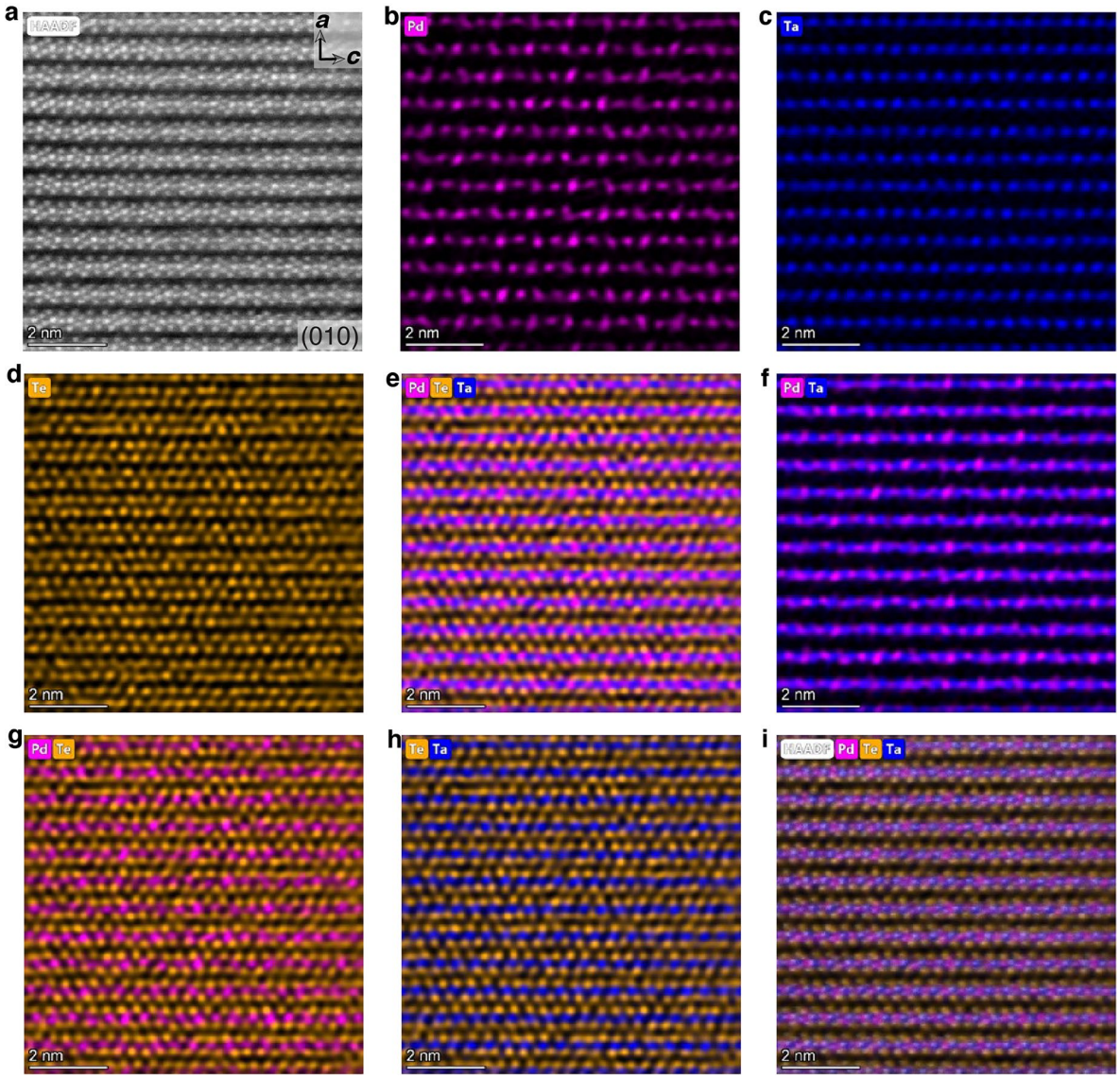

Extended Data Fig. 2 | Structure and phase characterization of $Ta_2Pd_3Te_5$. **a**, Atomic resolution image of the side surface of $Ta_2Pd_3Te_5$ (*that is*, 010 plane), obtained through scanning transmission electron microscopy, displaying a consistent atomic arrangement when compared to pristine $Ta_2Pd_3Te_5$. **b**–**i**, Elemental mappings of the side surface utilizing an energy dispersive X-ray detector. The mappings demonstrate the unperturbed atomic layers, highlighting the structural integrity and composition of $Ta_2Pd_3Te_5$.

https://doi.org/10.1038/s41567-025-02917-6

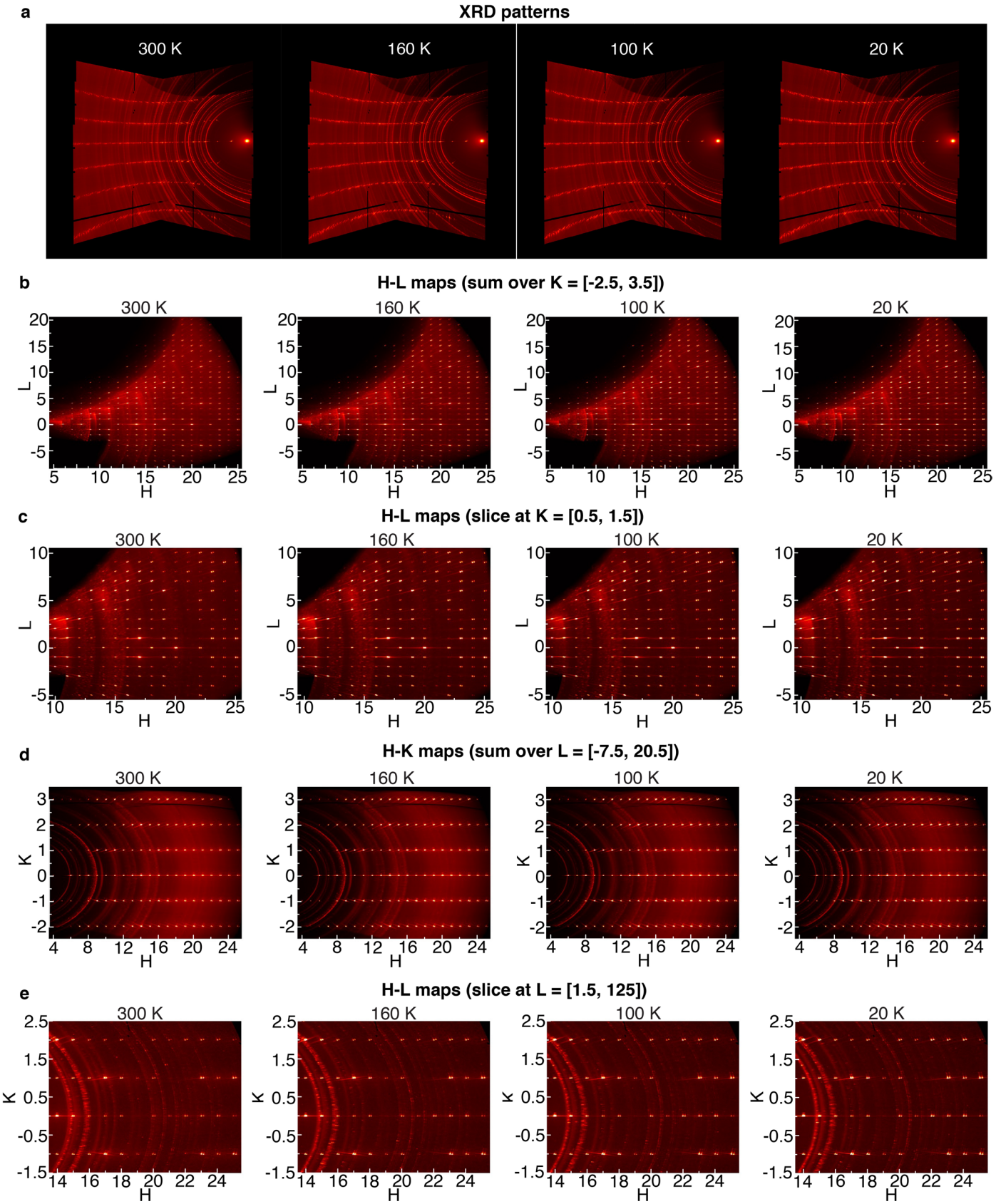

Extended Data Fig. 3 | X-ray diffraction measurements on $Ta_2Pd_3Te_5$ detecting no structural phase transition as a function of temperature. **a**, X-ray diffraction pattern measured at the same sample position for different temperatures ranging from 300 K to 20 K. **b**, Maps along the H-L direction obtained by summing over K= [−2.5, 3.5] and measured at four temperatures. **c**, Maps along H-L obtained by taking a slice at K = [0.5,1.5] measured at four temperatures. **d**, Maps along H-K obtained by summing over L = [−7.5, 20.5] and measured at four temperatures. **e**, Maps along H-K obtained by taking a slice at L = [1.5, 2.5]. Notably, there is no emergence of any new or additional peak at low temperatures. X-ray diffraction measurements consistently exhibit a good agreement with the *Pnma* crystal structure at all the measured temperatures.

https://doi.org/10.1038/s41567-025-02917-6

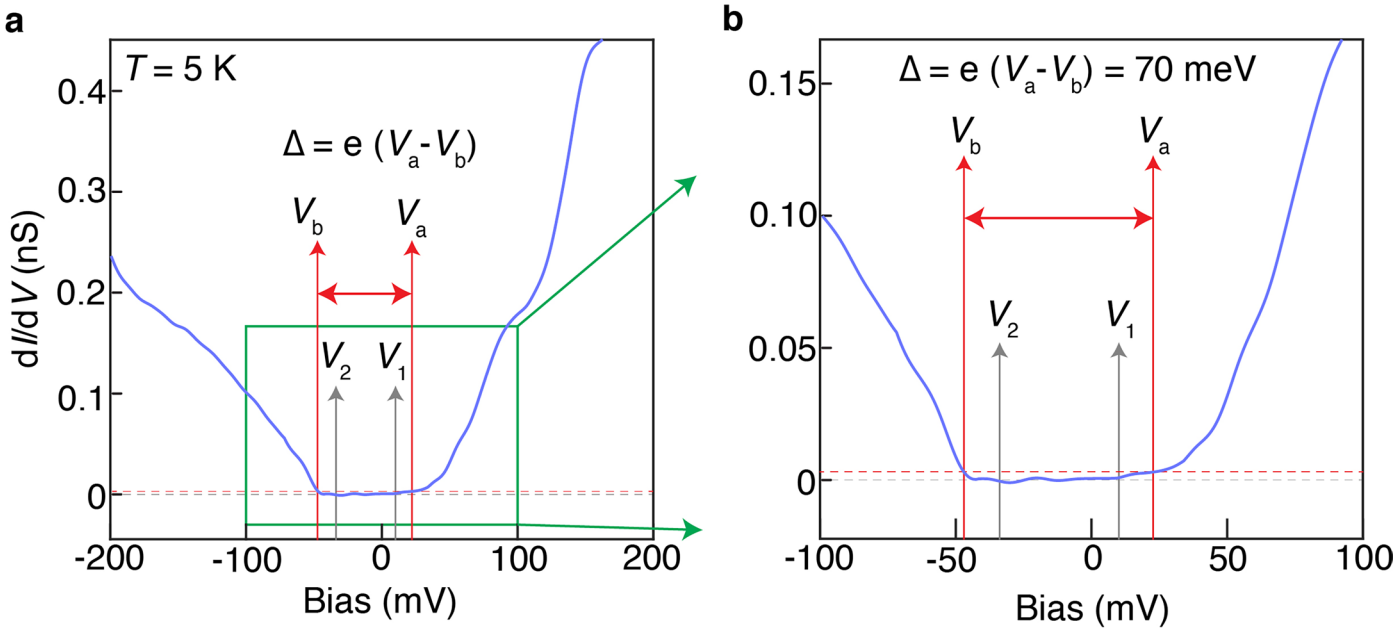

Extended Data Fig. 4 | Determination of the energy gap from tunneling spectroscopy. a, Averaged d*I*/d*V* spectrum acquired by tunneling into the *bc* plane of clean $Ta_2Pd_3Te_5$ at $T = 5$ K. The voltage interval $[V_1, V_2]$ is used to calculate the noise floor, σ. The dashed red line represents $\Gamma = 2.36\sigma$, which corresponds to the instrumental resolution of the d*I*/d*V* signal. V_a and V_b are the solutions of the equation $dI/dV = \Gamma$. The spectroscopic energy gap is calculated as $\Delta = eV_a - eV_b$, resulting in $\Delta \simeq 70$ meV. **b**, Magnified view of panel **a**, focusing on the gapped region in the averaged d*I*/d*V* spectrum.

https://doi.org/10.1038/s41567-025-02917-6

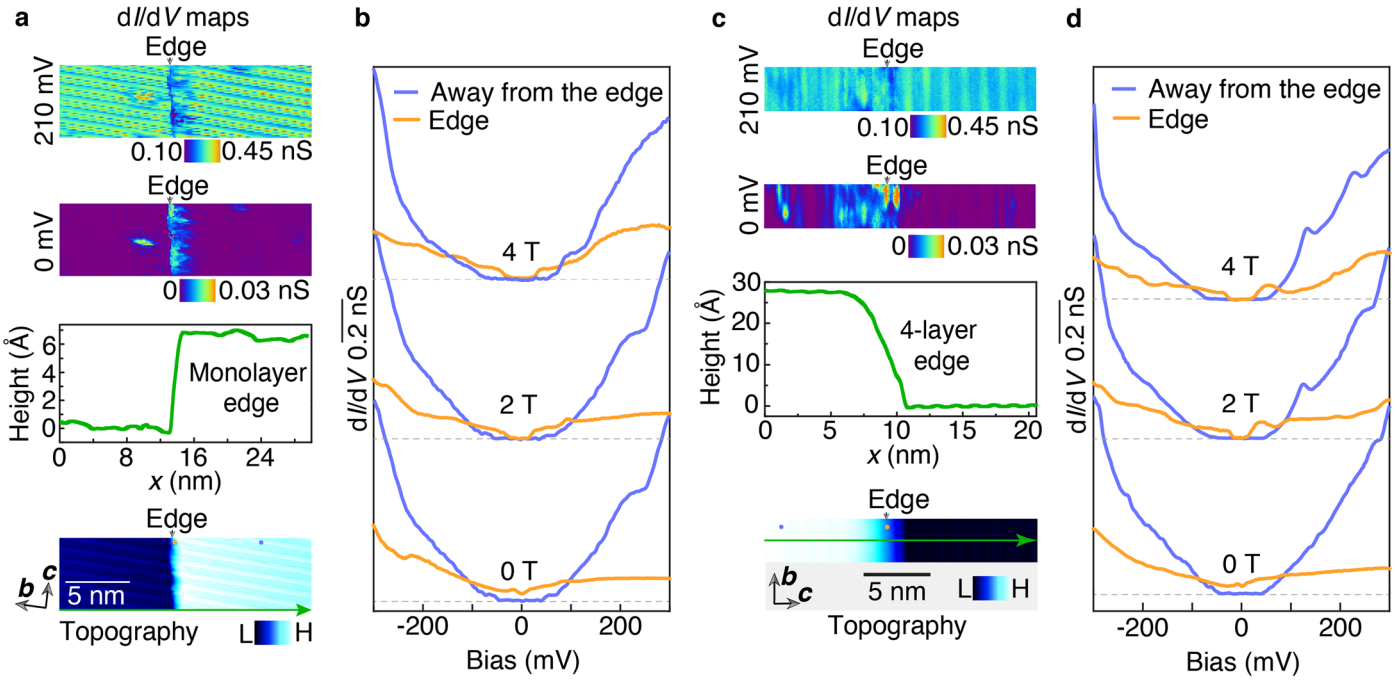

Extended Data Fig. 5 | Observation of time-reversal-symmetry-protected edge states for different edge configurations. a, d*I*/d*V* maps acquired at different bias voltages (corresponding topography is shown in the bottom panel) around a monolayer step edge parallel to the *c*-axis measured at $T = 5$ K. The height profile perpendicular to the *c*-axis is also displayed. The d*I*/d*V* map obtained within the energy gap ($V = 0$ mV) reveals a pronounced edge state, whereas at $V = 210$ mV, the edge state is suppressed. **b**, Tunneling spectra acquired at locations away from the step edge and on the step edge measured under various magnetic fields. The orange and violet curves represent the differential spectra obtained at the step edge and away from it, respectively. The corresponding spatial locations where the spectra are acquired are marked with color-coded dots on the topographic image in panel **a**. Spectra at different magnetic fields were collected at the same locations and are vertically offset for clarity. Dashed horizontal lines mark the zero d*I*/d*V* for different fields. **c**, d*I*/d*V* maps acquired at different bias voltages (corresponding topography is shown in the bottom panel) around a four-layer step edge parallel to the *b*-axis direction. The height profile perpendicular to the *b*-axis is also shown. The d*I*/d*V* map obtained within the energy gap ($V = 0$ mV) reveals a pronounced edge state, whereas at $V = 210$ mV, the edge state is suppressed. **d**, Tunneling spectra acquired at locations away from the step edge and on the step edge measured under various magnetic fields. The orange and violet curves represent the differential spectra taken at the step edge and away from it, respectively. The corresponding spatial locations where the spectra are acquired are marked with color-coded dots on the topographic image in panel **a**. Spectra at different magnetic fields were taken at the same locations and are vertically offset for clarity. Dashed horizontal lines mark the zero d*I*/d*V* for different fields. Tunneling junction set-up: $V_{set} = 300$ mV, $I_{set} = 0.5$ nA, $V_{mod} = 2$ mV.

https://doi.org/10.1038/s41567-025-02917-6

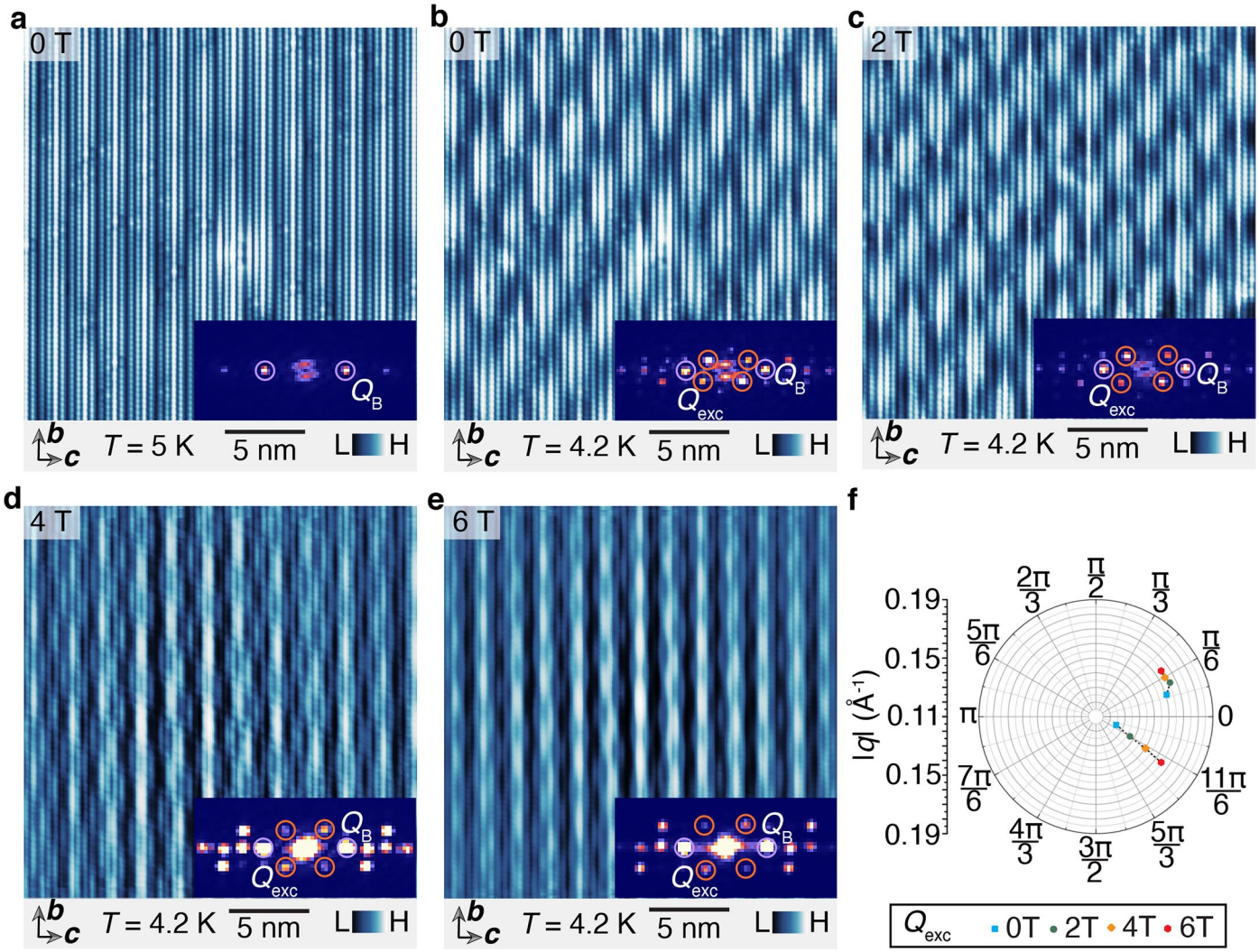

Extended Data Fig. 6 | Magnetic field tunability of the wavevector of the translational symmetry breaking order. a, Atomically resolved topographic image of a clean $Ta_2Pd_3Te_5$ (100) surface acquired at $T = 5$ K. Inset shows the corresponding Fourier transform image displaying well-defined Bragg peaks (purple circles). **b**, Topographic image of the same region presented in panel **a**, acquired at $T = 4.2$ K and $B = 0$ T, revealing a pronounced translational symmetry breaking order. Inset: Fourier transform image displaying well-defined superlattice peaks (orange circles) alongside the Bragg peaks (purple circles). The extracted wavevector is $Q_{exc} = [\ \pm(-0.43c^* + 0.035b^*), \pm(0.57c^* + 0.035b^*)\ ]$. **c**–**e**, Topographic images from the same location but acquired at magnetic fields of 2 T, 4 T, and 6 T, respectively, highlighting a change in the translational symmetry breaking ordering pattern upon increasing the magnetic field. The Fourier transform images shown in the inset reveal a gradually evolving $\mathbf{Q}_{exc}$ where $\mathbf{Q}_{exc}$ changes to $[\pm(-0.44c^* + 0.051b^*), \pm(0.56c^* + 0.051b^*)]$ at 2 T, $[\pm(-0.47c^* + 0.06b^*), \pm(0.53c^* + 0.06b^*)]$ at 4 T, and $\pm(0.5c^* + 0.07b^*)]$ at 6 T. **f**, Polar plot summarizing the magnetic field tunability of $\mathbf{Q}_{exc}$. Starting from being incommensurate along both b- and c-axes at $B = 0$ T, $\mathbf{Q}_{exc}$ evolves continuously and becomes commensurate along the c-axis at $B = 6$ T. Tunneling junction set-up: $V_{set} = 300$ mV, $I_{set} = 0.5$ nA.

https://doi.org/10.1038/s41567-025-02917-6

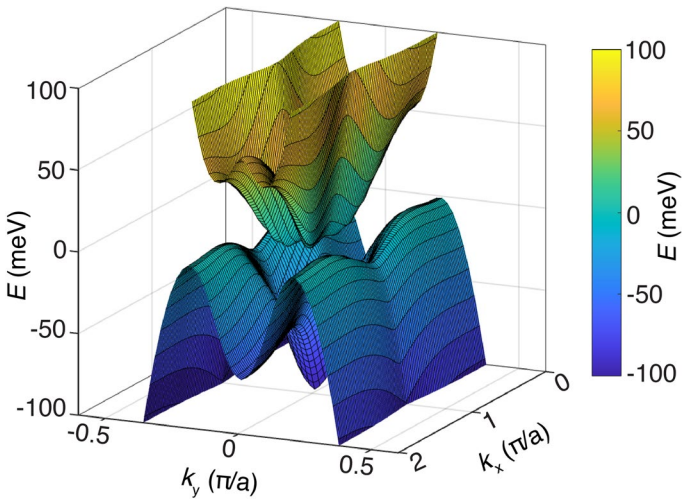

Extended Data Fig. 7 | Low-energy band structure of monolayer $Ta_2Pd_3Te_5$ obtained from first-principles calculations. Monolayer $Ta_2Pd_3Te_5$ exhibits semimetallic band structure.